A THEORETICAL STUDY OF STRAINED MONOLAYER TRANSITION METAL DICHALCOGENIDES BASED ON SIMPLE BAND STRUCTURES

A DISSERTATION SUBMITTED TO

THE GRADUATE SCHOOL OF ENGINEERING AND SCIENCE

OF BILKENT UNIVERSITY

IN PARTIAL FULFILLMENT OF THE REQUIREMENTS FOR

THE DEGREE OF

DOCTOR OF PHILOSOPHY

IN

PHYSICS

By

Shahnaz Aas

October 2019

A THEORETICAL STUDY OF STRAINED MONOLAYER TRANSITION METAL DICHALCOGENIDES BASED ON SIMPLE BAND STRUCTURES

By Shahnaz Aas

October 2019

We certify that we have read this dissertation and that in our opinion it is fully adequate, in scope and in quality, as a dissertation for the degree of Doctor of Philosophy.

Ceyhun Bulutay(Advisor)

Oğuz Gülseren

Cem Sevik

Bekir Sıtkı Kandemir

Balázs Hetényi

Approved for the Graduate School of Engineering and Science:

Ezhan Karaşan
Director of the Graduate School

ABSTRACT

A THEORETICAL STUDY OF STRAINED MONOLAYER TRANSITION METAL DICHALCOGENIDES BASED ON SIMPLE BAND STRUCTURES

Shahnaz Aas
Ph.D. in Physics
Advisor: Ceyhun Bulutay
October 2019

This doctoral thesis deals with optoelectronic and geometric band properties of two-dimensional transition metal dichalcogenides (TMDs) under applied strain. First, we analyze various types of strain for the K valley optical characteristics of a freestanding monolayer MoS_2, $MoSe_2$, WS_2 and WSe_2 within a two-band $k \cdot p$ method. By this simple bandstructure combined with excitons at a variational level, we reproduce wide range of available strained-sample photoluminescence data. According to this model strain affects optoelectronic properties. Shear strain only causes a rigid wavevector shift of the valley without any alternation in the bandgap or the effective masses. Also, for flexible substrates under applying stress the presence of Poisson's effect or the lack of it are investigated individually for the reported measurements. Furthermore, we show that circular polarization selectivity decreases/increases by tensile/compressive strain for energies above the direct transition onset.

TMDs in addition to their different other attractive properties have rendered the geometric band effects directly accessible. The tailoring and enhancement of these features by strain is an ongoing endeavor. In the second part of this thesis, we consider spinless two and three band, and spinful four band bandstructure techniques appropriate to evaluate circular dichroism, Berry curvature and orbital magnetic moment of strained TMDs. First, we establish a new $k \cdot p$ parameter set for MoS_2, $MoSe_2$, WS_2 and WSe_2 based on recently released ab initio and experimental band properties. For most of these TMDs its validity range extend from K valley edge to several hundreds of millielectron volts for both valence and conduction band. We introduce strain to an available three band tight-binding Hamiltonian to extend this over a larger part of the Brillouin zone. Based on these we report that by applying a 2.5% biaxial tensile strain, both the Berry curvature and the orbital magnetic moment can be doubled compared to their

unstrained values. These simple bandstructure tools can be suitable for the device modeling of the geometric band effects in strained monolayer TMDs.

Keywords: $k \cdot p$ Hamiltonian, excitons, Transition metal dichalcogenides, Strain, Photoluminescence, Circular dichroism, Berry curvature, Orbital magnetic moment.

ÖZET

TEK KATMANLI GERİNİMLİ GEÇİŞ METALİ KALKOJENİTLERİ İÇİN BASİT BANT YAPISINA DAYALI KURAMSAL BİR ÇALIŞMA

Shahnaz Aas
Fizik, Doktora
Tez Danışmanı: Ceyhun Bulutay
Ekim 2019

Bu tezin amacı iki boyutlu geçiş metali kalkojenitlerinin (GMD) uygulanan gerinim altında optoelektronik ve geometrik bant özelliklerinin incelenmesidir. Öncelikle iki bant $k \cdot p$ metodu kullanarak asılı MoS_2, $MoSe_2$, WS_2 ve WSe_2 tek katmanlarında K vadisi optik nitelikleri için birçok gerinim tipi incelendi. Bu basit bant yapısını kullanarak ve varyasyonel düzeyde exitonları hesaba katarak uygun gerinimli örnekler için geniş bir aralıkta benzer photoluminesence verisi elde ettik. Bu modele göre kayma gerinimi, band aralığında veya etkin kütlede hiçbir değişim içermeyerek vadi üzerinde sadece topluca bir dalga vektörü yerdeğişimine sebep olurken, hidrostatik bileşeni üzerinden optoelektronik özellikleri etkiler. Ayrıca esnek alttaşlarda Poisson etkisinin varlığı ya da yokluğu rapor edilen ölçümler için ayrı ayrı incelenmiştir. Buna ek olarak, dairesel kutuplaşma seçiciliğinin açıcı/büzücü gerinimi sayesinde direkt geçiş başlangıcı üstü enerjiler için bozulduğunu/iyileştiğini öngörüyoruz. GMDler diğer ilgi çekici özellikleri yanında geometrik band etkilerini vasıtasız mümkün kılmaktadır. Bu özelliğin gerinim kullanılarak ihtiyaca göre uyarlanması ve geliştirilmesi için çabalar devam etmektedir. İkinci bölümde gerinimli GMDlerin dairesel çiftrenklilik, Berry eğriliği ve yörünge manyetik momentini değerlendirmek için spinsiz iki, üç bant ve spinli dört bant bantyapı yöntemlerinden uygun olanı kullandık. Öncelikle MoS_2, $MoSe_2$, WS_2 ve WSe_2 için yakında yayınlanmış olan ab initio ve deneysel bant özelliklerine dayanan yeni bir $k \cdot p$ parametre seti tespit ettik. Setin geçerlilik aralığı bu GMDlerin büyük çoğunluğunda hem değerlik ve hem de iletim bandı için K vadisi kenarından birkaç yüz milielektronvolt yukarısına uzanmaktadır. Bunu Brillouin bölgesinin daha geniş bir kısmına yaymak amacıyla mevcut üç bant sıkı bağ Hamiltonyene gerinim ilave ettik. Bunlara dayanarak; çift eksenli 2.5% çekme gerinimi uygulanması durumunda hem Berry eğriliği hem de yörünge manyetik momenti gerinimsiz değerlerine oranla ikiye katlanabileceğini gösterdik.

Bu geliştirilmiş basit bant yapı gereçleri, gerinimli GMD tek katmanlarında geometrik band etkilerinin aygıt modellemesi için uygun olabilir.

Anahtar sözcükler: $k \cdot p$ Hamiltonyen, egziton, geçiş metali kalkojenitleri, gerinim, fotoışıma , dairesel çiftrenklilik, Berry eğriliği, yörünge manyetik momenti.

Acknowledgement

Firstly, I would like to express my sincere gratitude to my advisor Prof. Ceyhun Bulutay for the continuous support of my Ph.D study and related research, for his patience, motivation, and immense knowledge. His guidance helped me in all the time of research and writing of this thesis.

Besides my advisor, I would like to thank the rest of my thesis committee: Prof. Oguz Gulseren, Prof. Cem Sevik, Prof. Bekir Sıtkı Kandemir and Assist. Prof. Balázs Hetényi for their insightful comments and encouragement, but also for the hard question which incented me to widen my research from various perspectives.

I would like to acknowledge financial support of Bilkent university, department of physics.

The special thanks goes to my husband, Muammer for his patience and support during the PhD period.

Contents

List of Figures

List of Tables

Chapter 1

Introduction

The research on two-dimensional (2D) transition metal dichalcogenide (TMD), semiconductors of the type MX_2, where M is a transition metal atom (such as Mo or W) and X is a chalcogen atom (such as S, Se or Te) [1], recently has attracted significant interest [1, 2, 3, 4, 5, 6]. They exhibit a unique combination of atomic-scale thickness, direct bandgap, strong spin-orbit coupling and favorable electronic and mechanical properties, making them attractive for fundamental studies and applications. Two dimensionality of the TMDs along with weak dielectric screening from its environment yield a significant enhancement of the Coulomb interaction that directly affect the excitonic and trionic properties. As a result of the enhanced excitonic effect in two dimensions, these materials host extremely strong light-matter interactions [7, 8]. In addition, control of these excitons is possible by optical, electrical and mechanical means [9, 10]. Mechanical flexibility is a unique advantage for 2D materials [11]. The electronic band structure strongly depends on the lattice constant. Hence, it varies with a mechanical strain, as well. Therefore, optical properties, especially interband transitions and resultant excitonic and trionic properties are expected to vary with strain. By applying an uniaxial tensile strain to monolayer MoS_2 on flexible substrates, the continuous tuning of the electronic structure is observed by He et al.[9]. Similar results were reported by Conley and co-workers [12]. More recent study from Lloyd et al. shows that continuous and reversible tuning of the optical band gap for a

suspended monolayer MoS_2 membrane is possible under ultralarge applied biaxial strain [13]. Some other experimental [9, 12, 14, 5, 15, 16, 17, 18, 19, 20, 21, 22] as well as theoretical [23, 24, 25, 26, 27, 28, 29, 30, 31, 32, 33, 34, 35, 36, 37, 38] works exist which shows effects of strain as a viable control mechanism of neutral excitons and trions inside of these 2D materials. Also, Palacios-Berraquero et al. [39] and Branny et al. [40] in different works has been reported the emergence of quantum emmiters from thin TMDs as a direct effect of strain. All these studies and more confirm that this feature makes 2D materials a very promising candidate for future optoelectronic devices.

1.0.1 Excitons and Trions of TMDs

When a photon is absorbed by a semiconductor, it excites an electron from the valence band into the conduction band. In turn, this leaves behind a positively charged hole. The electron in the conduction band is then electrostatically attracted to this free hole. This quasiparticle is called an exciton with an energy level slightly lower than the energy of excitation. Due to strong Coulomb interaction in TMDs, the amount of exciton binding energy is considerably higher than the value for typical bulk semiconductors such that in TMDs, exciton binding energies are on the order of 500 meV [41, 42, 8], while for Wannier excitons in traditional semiconductor it is around 10 meV [43].

When a neutral exciton captures an additional free electron or a hole such a complex is called negative trion (containing one negative charge and one exciton) or positive trion (containing one positive charge and one exciton). The trion binding energy is defined as the energy required to separate the trion into a free exciton and a free charge, which is considerably less than the exciton binding energy. This comes from the overall attractive interaction between the extra charge and exciton. Because of higher effective mass (lower energy) for free electrons or holes in TMDs, trion binding energy for these materials can be just defined as trion energy minus free exciton energy as shown schematically in Fig. 1.1.

Notably, the amount of trion binding energy in TMDs is about one order of magnitude larger than their counterparts in quantum wells (20 meV for MoS_2). This allows the observation of trions for MoS_2 even at room temperature [7] while it can be observed in quantum wells only at very low temperatures[44, 45].

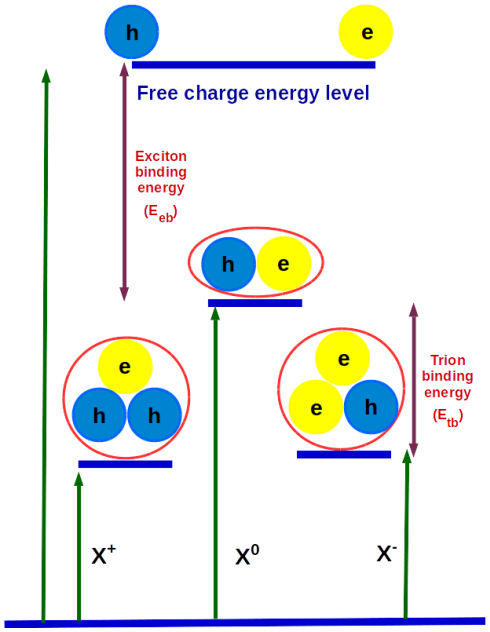

Figure 1.1: Schematic of Trions. The trion binding energy is defined as the energy difference between the trion energy and the neutral exciton.

1.0.2 Valley Excitons of TMDs

TMDs break inversion symmetry for odd number of layers (including monolayer) but is restored the symmetry in even numbered layers as shown in Fig. 1.2 (a). (Image is taken from Ref. [46]). This broken inversion symmetry in monolayer TMDs makes them an ideal system to realize valley polarization [47]. The bands at the K (-K) points are splitting with the opposite spins because of spin-orbit coupling and time reversal symmetry. This effect is shown in Fig. 1.2 (b). (Image is taken from Ref. [46]). Liu et al. experimentally demonstrated valley-dependent circular dichroism through excitation of the K $(-K)$ valley with $\sigma-$ $(\sigma+)$ light to yield PL of the same polarization in MoS_2 (Fig. 1.2 (c)). (Image is taken from

Ref. [48]).

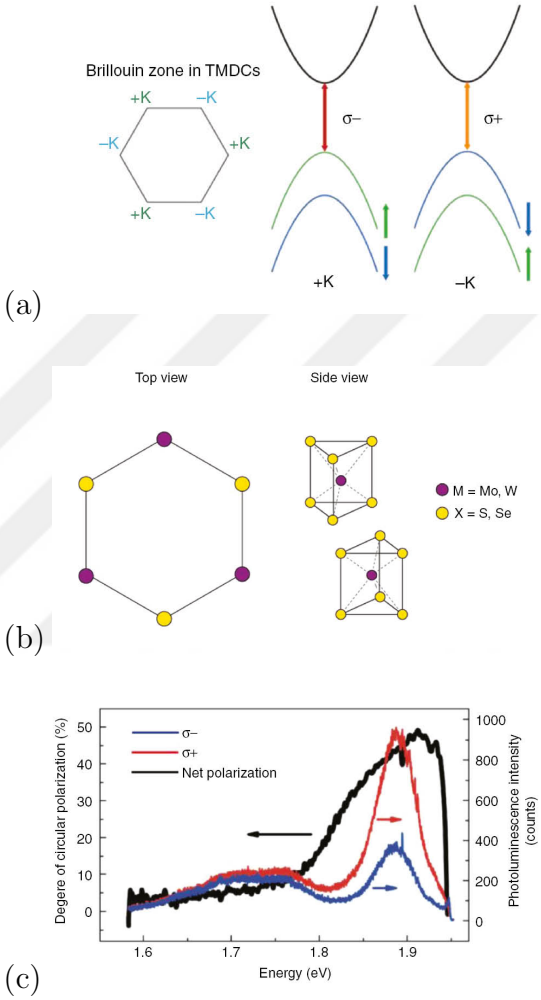

Figure 1.2: (a) Crystal structure in TMD materials. The top view of the crystal is hexagonal. Transition metals are sandwiched between two layers of chalcogen atoms. The inversion symmetry within one layer is broken but restored upon even layers. (b) Schematic of electron bands near the K points of the Brillouin zone. (c) Circular dichroism in MoS_2. (Image is taken from Ref. [48]).

1.0.3 Strain Effects on Excitonic and Valleytronic Properties of TMDs

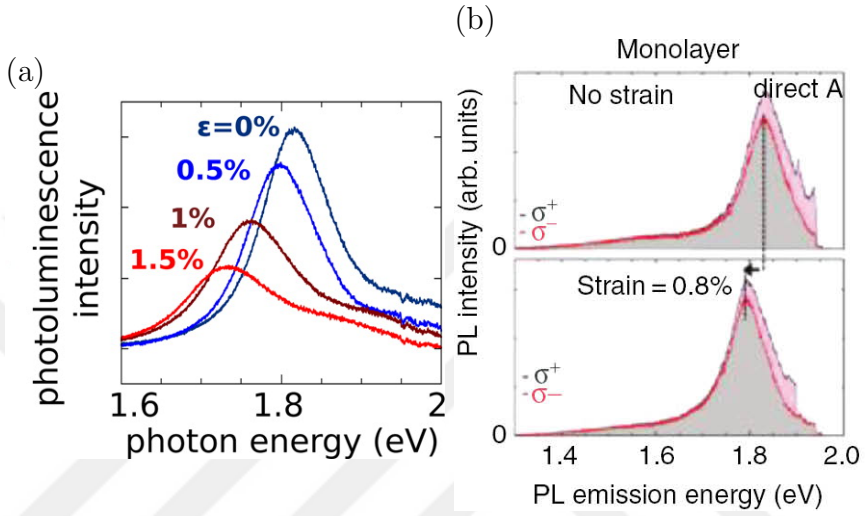

Figure 1.3: (a) Photoluminescence of strained monolayer MoS_2. PL emission intensity decreases by applying strain and peak position shifts toward lower energy. (b) PL emission for a monolayer MoS_2 without and with 0.8% strain for $\sigma+$ and $\sigma-$ polarization. (Image is taken from Ref. [5]).

Mechanical flexibility is a unique advantage for 2D materials [11]. The electronic band structure is strongly dependent on the lattice constant. Hence, it varies with a mechanical strain, as well. Therefore, optical properties, especially interband transitions and resultant excitonic and trionic properties are expected to vary with strain. By applying an uniaxial tensile strain to monolayer MoS_2 on flexible substrates, the continuous tuning of the electronic structure is observed by He et al.[9]. Similar results were reported by Conley and co-workers [12]. They also showed that the photoluminescence (PL) energy has 45 meV decrease per percent strain for monolayer MoS_2 Fig. 1.3 (a). (Image is taken from Ref. [12]).

Furthermore, strain can influence valley polarization as well as electronic band structure in TMDs. Strong decrease of PL helicity for both monolayer and bilayer MoS_2 samples has been reported by applying a strain up to 0.8 %, as shown in

Fig. 1.3 (b). (Image is taken from Ref. [5]).

1.0.4 Geometrical Band Effects in TMDs

In TMDs the valley degree of freedom is an individually addressable quantum label [49], unlike the conduction band valleys in regular bulk silicon. Their valley-contrasting features associated with the so-called inequivalent K valleys at the edges of hexagonal Brillouin zone provide carriers that can enjoy non-dissipative electronics [50].

From the quantum geometrical band properties aspect [51], these phenomena can be related to the Berry curvature (BC) and orbital magnetic moment (OMM) [52]. These contribute in various phenomena such as the dichroic selection rules in optical absorption [53, 54], or the excitonic p level energy splitting that is corresponding to the BC flux [55, 56]. OMM elucidates the interatomic currents (self-rotating motion of the electron wavepacket) [57] which is responsible for the valley g-factor in TMDs [58, 59]. Thus, by breaking time-reversal symmetry with a perpendicular magnetic field, in addition to the well-known spin Zeeman effect a valley Zeeman splitting is introduced as well [60, 55]. Very recently, these geometric band properties have been locally mapped in momentum space using circular dichroism angle-resolved photoelectron spectroscopy, through their intimate connection with the orbital angular momentum [61].

Also the valley dependent Berry phase effect can result in a valley contrasting Hall transport such that carriers in different valleys fllow in opposite directions transverse to an in-plane electric field E_y. The apperearing Hall current is given by [62],

$$j_x = \frac{e^2}{h}\left[\frac{f_1}{2\bar{\mu}^2} - \frac{9 f_1 f_2^2 \bar{q}_F^2 a^2}{8\bar{\mu}^4}\right]\delta\mu E_y, \tag{1.1}$$

where q_F is the Fermi wave vector which is related to the bulk chemical potential by $\mu = \frac{1}{2}\sqrt{f_1^2 + 3q_f^2 a^2 f_2^2}$. Fig. 1.4 shows this phenomenon scematically. (Image is taken from Ref. [63]). This effect can be used to create and detect valley polarization by magnetic and electric tools, forming the basis for the valley-based

electronics applications.

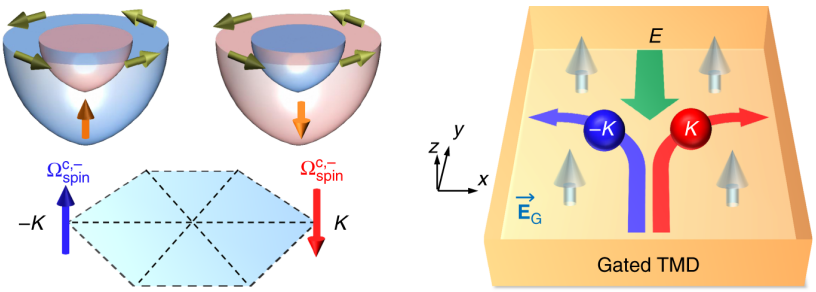

Figure 1.4: Electric generation of the valley polarization. An in-plane electric field generates a transverse valley current, that leads to a net valley polarization on the sample edges. (Image is taken from Ref. [63]).

1.1 This Work

This thesis theoretically scrutinizes the effects of applied strain on monolayer TMD samples with the aid of a simple K-valley-specific two-band $k \cdot p$ theory. In Chapter 2, this two-band strained $k \cdot p$ approach for TMDs is introduced first. A discussion on the electronic band structure of these monolayer materials under different types of applied strain is provided in this chapter as well. Chapter 3 contains effect of strain on circular dichroism (CD) and PL peak shift in detail. In Chapter 4 we propose an effective two-band $k \cdot p$ approach including electron-hole symmetry breaking and trigonal warping effect. We used this new Hamiltonian to see how these terms affect energy dispersion, effective mass and CD for a monolayer MoS_2. Last in this Chapter the effect of strain on CD is explored. In Chapter 5 geometrical band properties in strained TMDs is discussed using simple band structures. Here, a new parameter set is developed for a (two − or four band) $k \cdot p$ model as well as a strained extension for a three-band TB Hamiltonian. Chapter 6 concludes our results and give some prospective points for the future work of this research.

Chapter 2

Strain Dependence of Excitonic Properties in TMDs

Applying strain on monolayer TMDs influences their optical fingerprint, including excitonic binding energy. Feierabend et al. present an analytical view on this feature, combining microscopic theory based on Wannier and Bloch equations with nearest-neighbor tight-binding approximation [38]. Fang et al. provide a two-band strained $k \cdot p$ Hamiltonian to explore the effect of strain on TMDs in the vicinity of K valley [64]. Sec. 2.1 of this chapter describes their models in detail. Strain tensors for different types of (uniaxial/biaxial and shear) strain are discussed in this section as well. Furthermore, simple analytical forms are produced for energy bands, band gap and excitonic effective mass of TMDs under applied strain. Sec. 2.2 contains the dispersion curve for different TMDs under various types of strain along with the extremum points for conduction/valence bands. Furthermore, in Sec. 2.3 the band gap behavior as well as the change of exciton effective mass are given under any special type of strain.

2.1 Two-Band Strained $k \cdot p$ Approach in TMDs

Fang et al. constructed the tight-binding Hamiltonian for monolayer TMD in the presence of strain [64]. It consists of seven valence bands and four conduction bands which are hybrids of metal d orbitals and chalcogen p orbitals. Fang et al. in the same article [64] altered the spinless full 11-band tight-binding model [65, 33] for TMDs to the reduced two-band model at the $K+$ point, consisting of the highest valence band ϕ^v (of $d_{x^2-y^2}+id_{xy}$ character) and the lowest conduction band ϕ^c (of d_z^2 character). The presented effective $k \cdot p$ Hamiltonian for the unstrained TMD is given by:

$$H_0 = f_0\mathbb{1} + \frac{f_1}{2}\hat{\sigma_z} + f_2 a(k_x\hat{\sigma_x} + k_y\hat{\sigma_y}), \tag{2.1}$$

where a is the lattice constant, σ_i's are Pauli spin matrices and f_i's are the strained $k \cdot p$ parameters. f_i's are fitted to the first-principles electronic bandstructure which are for convenience listed in Table. 2.1 [64]. By defining additional strain terms in the Hamiltonian as,

$$H_{strain} = f_3 \sum_i \varepsilon_{ii}\mathbb{1} + f_4 \sum_i \varepsilon_{ii}\hat{\sigma_z} + f_5\big[(\varepsilon_{xx} - \varepsilon_{yy})\hat{\sigma_x} - 2\varepsilon_{xy}\hat{\sigma_y}\big]). \tag{2.2}$$

the strained $k \cdot p$ Hamiltonian matrix can be expressed as

$$H = H_0 + H_{strain} = \begin{bmatrix} \big(f_0 + \frac{f_1}{2}\big) + (f_3 + f_4)(\varepsilon_{xx} + \varepsilon_{yy}) & f_2 a(k_x - ik_y) + f_5(\varepsilon_{xx} - \varepsilon_{yy} + 2i\varepsilon_{xy}) \\ f_2 a(k_x + ik_y) + f_5(\varepsilon_{xx} - \varepsilon_{yy} - 2i\varepsilon_{xy}) & \big(f_0 - \frac{f_1}{2}\big) + (f_3 - f_4)(\varepsilon_{xx} + \varepsilon_{yy}) \end{bmatrix} \tag{2.3}$$

where $f_3(f_4)$ is modifying the midgap position (massive gap), and f_5 is the pseudo gauge field term, In Eq. (2.3) we refer to K_+ valley, that is supposed to be the wavevector origin $\vec{k} = \hat{x}k_x + \hat{y}k_y$, with k_x pointing along the $\Gamma - K$ direction. Our treatment excludes other refinements such as trigonal warping, electron-hole asymmetry, and a cubic deviation in the band structure [66]. These will be incorporated in Chapter. 4 of this thesis.

Table 2.1: $k \cdot p$ parameters f_i (eV), lattice constant a (Å) [64], 2D polarizability χ_{2D} (Å)[67] for different TMDs.

Materials	f_0	f_1	f_2	f_3	f_4	f_5	a	χ_{2D}
MoS_2	-5.07	1.79	1.06	-5.47	-2.59	2.2	3.182	6.60
$MoSe_2$	-4.59	1.55	0.88	-5.01	-2.28	1.84	3.317	8.23
WS_2	-4.66	1.95	1.22	-5.82	-3.59	2.27	3.182	6.03
WSe_2	-4.23	1.65	1.02	-5.26	-3.02	2.03	3.316	7.18

Strain tensor is defined as,

$$\varepsilon_{ij} = \frac{1}{2}\left(\frac{\partial u_i}{\partial x_j} + \frac{\partial u_j}{\partial x_i}\right) \tag{2.4}$$

$$= \begin{bmatrix} \varepsilon_{xx} & \varepsilon_{xy} & \varepsilon_{xz} \\ \varepsilon_{yx} & \varepsilon_{yy} & \varepsilon_{yz} \\ \varepsilon_{zx} & \varepsilon_{zy} & \varepsilon_{zz} \end{bmatrix}$$

$$= \begin{bmatrix} \frac{\partial u_x}{\partial x} & \frac{1}{2}\left(\frac{\partial u_x}{\partial y} + \frac{\partial u_y}{\partial x}\right) & \frac{1}{2}\left(\frac{\partial u_x}{\partial z} + \frac{\partial u_z}{\partial x}\right) \\ \frac{1}{2}\left(\frac{\partial u_y}{\partial x} + \frac{\partial u_x}{\partial y}\right) & \frac{\partial u_y}{\partial y} & \frac{1}{2}\left(\frac{\partial u_y}{\partial z} + \frac{\partial u_z}{\partial y}\right) \\ \frac{1}{2}\left(\frac{\partial u_z}{\partial x} + \frac{\partial u_x}{\partial z}\right) & \frac{1}{2}\left(\frac{\partial u_z}{\partial y} + \frac{\partial u_y}{\partial z}\right) & \frac{\partial u_z}{\partial z} \end{bmatrix}$$

where, diagonal terms are strain components in three dimensions and off diagonal terms are shear components. For 2D TMDs there is no component in z direction. So, strain tensor has the form,

$$\begin{bmatrix} \varepsilon_{xx} & \varepsilon_{xy} \\ \varepsilon_{yx} & \varepsilon_{yy} \end{bmatrix} \tag{2.5}$$

$$= \begin{bmatrix} \frac{\partial u_x}{\partial x} & \frac{1}{2}\left(\frac{\partial u_x}{\partial y} + \frac{\partial u_y}{\partial x}\right) \\ \frac{1}{2}\left(\frac{\partial u_y}{\partial x} + \frac{\partial u_x}{\partial y}\right) & \frac{\partial u_y}{\partial y} \end{bmatrix},$$

where, diagonal terms corresponds to strain effects and off diagonal terms corresponds to shear effects. For biaxial strain ε_{yy} equals to ε_{xx} as strain is applied

from both sides at the same rate while as an uniaxial stress is applied along x direction. The amount of created strain in y direction can be determined by Poisson's ratio as below,

$$\nu = -\frac{[lateral\ strain]}{[strain\ in\ the\ direction\ of\ applied\ uniaxial\ stress]} = -\frac{\frac{\partial u_y}{\partial y}}{\frac{\partial u_x}{\partial x}} = -\frac{\varepsilon_{yy}}{\varepsilon_{xx}}. \tag{2.6}$$

Positive ν means that the amount of stress in lateral position is in opposite sign with applied strain. All strain and shear effects can be summarized as below,

$$\begin{aligned}
\text{Biaxial strain :} \quad & \varepsilon_{yy} = \varepsilon_{xx}, \quad \varepsilon_{xy} = \varepsilon_{yx} = 0, \\
\text{Uniaxial strain :} \quad & \varepsilon_{xx} \neq 0, \quad \varepsilon_{yy} = \varepsilon_{xy} = \varepsilon_{yx} = 0, \\
\text{Shear strain :} \quad & \varepsilon_{yy} = -\varepsilon_{xx}, \quad \varepsilon_{xy} = \varepsilon_{yx} \neq 0, \\
\text{Uniaxial stress :} \quad & \varepsilon_{yy} = -\nu\varepsilon_{xx}, \quad \varepsilon_{xy} = \varepsilon_{yx} = 0,
\end{aligned}$$

Poisson's ratios for different TMDs are calculated both theoretically and experimentally [68, 69, 70, 71, 72, 73, 74]. The tensor strain components for biaxial, uniaxial and shear types are:

$$\begin{bmatrix} \varepsilon_{xx} & 0 \\ 0 & \varepsilon_{xx} \end{bmatrix}, \tag{2.7}$$

$$\begin{bmatrix} \varepsilon_{xx} & 0 \\ 0 & -\nu\varepsilon_{xx} \end{bmatrix}, \tag{2.8}$$

and

$$\begin{bmatrix} \varepsilon_{xx} & \varepsilon_{xy} \\ \varepsilon_{xy} & -\varepsilon_{xx} \end{bmatrix}, \tag{2.9}$$

respectively. The term uniaxial *strain* is in widespread use in TMD literature [12, 75, 21, 22], although with the assumed Poisson's effect, it should be referred to as uniaxial *stress*; also note that we use tensor and not the engineering strain [76].

Some strained $k \cdot p$ expressions can be obtained analytically from Eq. (2.3): The direct bandgap becomes,

$$E_g \equiv f_1 + 2f_4(\varepsilon_{xx} + \varepsilon_{yy}). \tag{2.10}$$

To simplify this equation, also we make use of the (areal) hydrostatic component of strain, $\varepsilon_H = \varepsilon_{xx}+\varepsilon_{yy}$. If we define $k_{x0} \equiv (\varepsilon_{xx}-\varepsilon_{yy})f_5/(f_2 a)$, $k_{y0} \equiv 2\varepsilon_{xy}f_5/(f_2 a)$, and $q_x \equiv k_x - k_{x0}$, $q_y \equiv k_y - k_{y0}$, with their magnitude $q = \sqrt{q_x^2 + q_y^2}$, then the energy dispersion for the conduction and valence bands are given by

$$\begin{aligned} E_{c/v}(k_x, k_y) &= f_0 + f_3(\varepsilon_{xx} + \varepsilon_{yy}) \pm \frac{E_g}{2}\sqrt{1 + \frac{(2f_2 a)^2}{E_g^2}\left[(k_x - k_{x0})^2 + (k_y - k_{y0})^2\right]} \\ &= f_0 + f_3\varepsilon_H \pm \frac{E_g}{2}\sqrt{1 + 4\left[r(q, \varepsilon_H)\right]^2} \end{aligned} \tag{2.11}$$

in terms of an auxiliary function that depends on the wavenumber (valley edge-centered) and the hydrostatic strain as

$$r(q, \varepsilon_H) \equiv \frac{f_2 a q}{f_1 + 2f_4\varepsilon_H}. \tag{2.12}$$

Hence, the valley edge shifts from $(k_x = 0, k_y = 0)$ to (k_{x0}, k_{y0}) because of strain. So that for $\varepsilon_{xx} > \varepsilon_{yy}$, $k_{x0} > 0$, and band extremum at K shifts toward M' point, while for $\varepsilon_{yy} > \varepsilon_{xx}$, $k_{x0} < 0$ it shifts toward Γ point. The shear strain dose not effect the bandgap while rigidly displaces band extremum along k_y direction. g7eis78ew3jredukcjumnhcdyjreusmjydcjwdejrthvfdvc40oiftrddfdskijyfngrft The eigenvectors of the two-band Hamiltonian in Eq. (2.3) corresponding to the conduction and valence states are given by

$$|U_c\rangle = \begin{pmatrix} x_1 \\ x_2 \end{pmatrix}, \quad |U_v\rangle = \begin{pmatrix} x_2 \\ -x_1^* \end{pmatrix}, \tag{2.13}$$

where in terms of $\phi = \tan^{-1}(q_y/q_x)$, an r defined in Eq. (2.12) the entries are given by

$$x_1 = \frac{e^{-i\phi}}{\sqrt{1 + r^2}}, \tag{2.14}$$

$$x_2 = \frac{r}{\sqrt{1 + r^2}}. \tag{2.15}$$

Also, we extract the valley edge effective masses $m^*_{c/v}$ from the energy dispersion relation (Eq. (2.11)) via,

$$m^*_{c/v} = \frac{\hbar^2}{\left(\frac{\partial^2 E_{c/v}}{\partial k^2}\Big|_{k_{x0}, k_{y0}}\right)} = \pm\frac{\hbar^2\left(f_1 + 2f_4\varepsilon_H\right)}{2(f_2 a)^2}, \tag{2.16}$$

where the curvatures are evaluated at the strained band extremum, (k_{x0}, k_{y0}). Here, electron and hole effective masses are equal, i.e., $m_e^* = m_c^* = m_h^* = -m_v^*$, and spatially isotropic but they are strain-dependent. Thus, the corresponding exciton effective mass follows from $\mu = m_e^* m_h^* / (m_e^* + m_h^*)$.

2.2 Electronic Band Structure of TMDs Under Strain

The top valence band as well as bottom conduction band is plotted for different TMDs under various types of applied strain by using of Eq. 2.11. Here, we used the quantities for Poisson's ratio listed in Table. 2.2 from Ref. [74].

Table 2.2: Poisson's ratio for different TMDs [74]

Materials	MoS_2	$MoSe_2$	WS_2	WSe_2
ν	0.24	0.23	0.21	0.19

Fig. 2.1, 2.2 and 2.3 shows effects of uniaxial and biaxial strain as well as shear effect on dispersion bands of different TMDs, respectively.

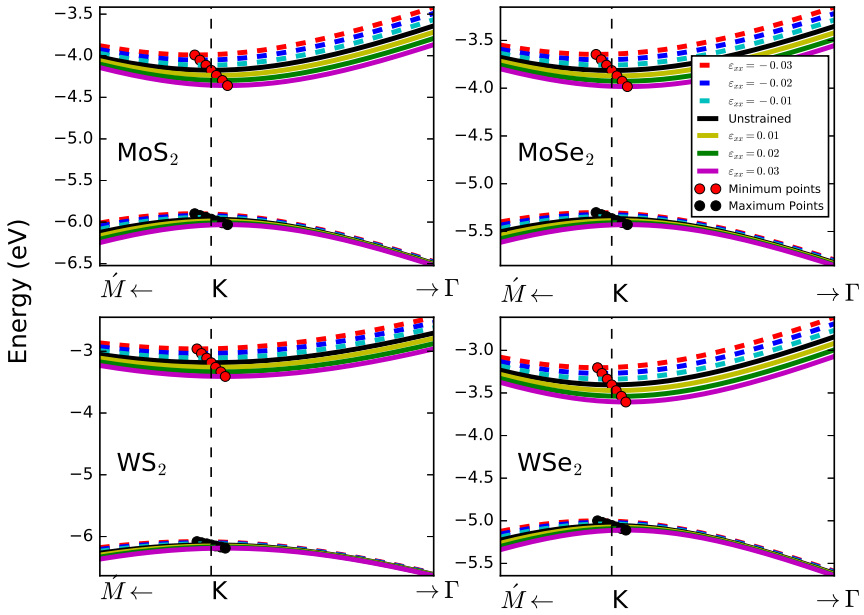

Figure 2.1: Effect of uniaxial strain on energy band-gap of TMDs for different amount of applied compressive and tensile strain.

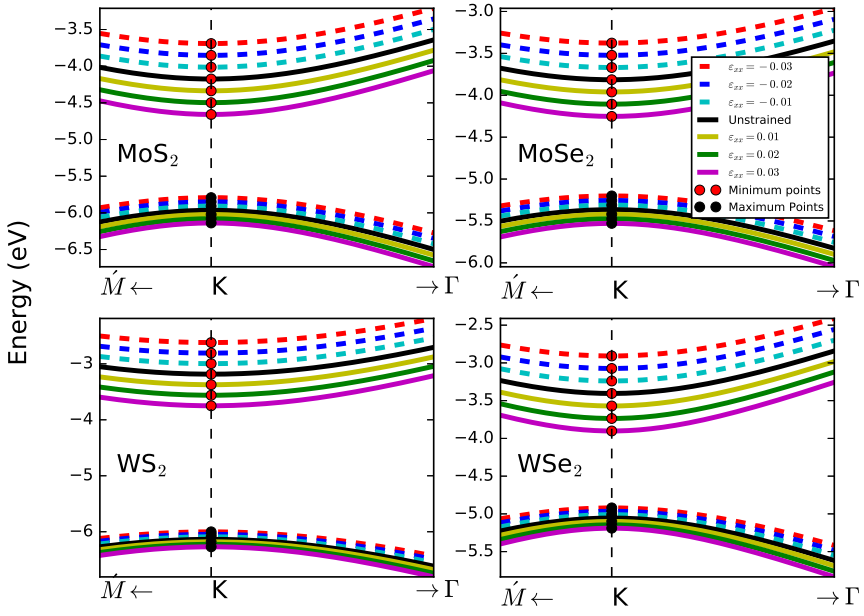

Figure 2.2: Effect of biaxial strain on energy band-gap of TMDs for different amount of applied compressive and tensile strain.

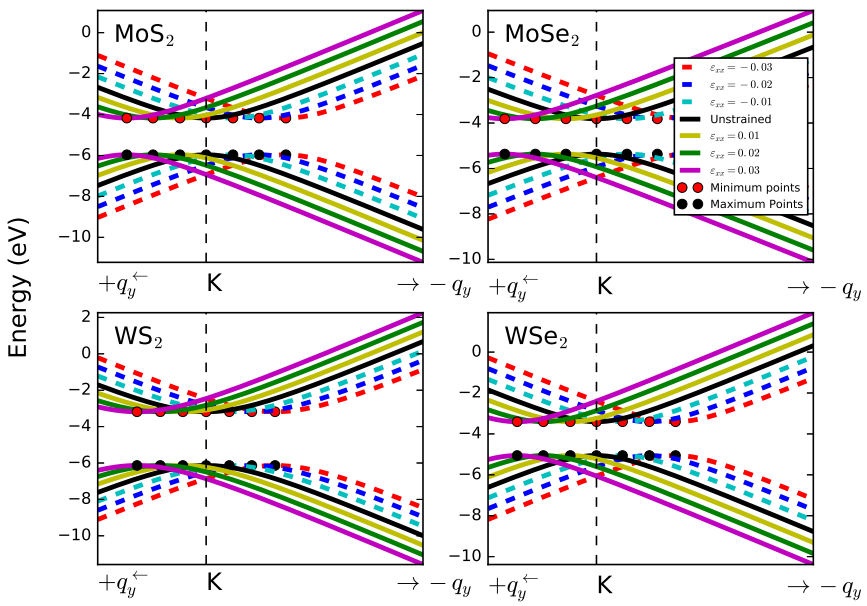

Figure 2.3: Shear effect on energy band-gap of TMDs. Positive and negative amount are for direction of applies shear only.

Furthermore, The absolute minimum (maximum) point for each conduction (valence) band is indicated by red (black) dots in the figures. To detect absolute min (max) points for any dispersion curve in each plot, we had to choose correct path in reciprocal lattice. To do that, we found the min (max) coordinate point of any dispersion curve by tracking all directions in reciprocal lattice. We got that, for uniaxial and biaxial strain these points would be on k_x axis for small amount of compressive or tensile strain, while they are on k_y axis for small amount of applied shear. Fig. 2.4 shows these results schematically. Here, we used quantity of 0.2 as applied strain or shear to be able to see the crystal changes schematically. By all these information in hand, we chose k_x direction to plot energy dispersion band of TMDs under uniaxial and biaxial strain as well as k_y direction to plot them under shear effect. Fig. 2.4 and Fig. 2.1 tells us that the min (max) energy for conduction (valence) band will not be in K+ point of the deformed reciprocal lattice under uniaxial strain. This comes from the fact that uniaxial strain breaks the symmetry of crystal. Thus, the min (max) point would be sliding in respect to the deformed crystal K+ point. As it can be seen from Fig. 2.1 that min (max)

point slides toward Γ point for a tensile strain while it goes through $\acute{M}$ point for a compressive strain amount. Fig. 2.2 shows that this is not the case for biaxial strain. Here, min (max) point is fixed at K+ point because the crystal symmetry does not change in this case. Finally, Fig. 2.3 shows that min (max) point slides toward positive or negative side in k_y direction for a positive or negative shear amount. This happens because shear breaks down the symmetry of the crystal as well. Furthermore, from figures. 2.1 and 2.2, both conduction and valence bands peak position is shifted from their unstrained position under tensile (uniaxial and biaxial) strain. Also, band energies decrease for tensile (uniaxial and biaxial) strain, while increase for compressive strain, causing a big change in energy band gap in both cases. For shear strain from Fig. 2.3 it can be seen that band energies are almost unchanged but, the peak positions are shifted in armchair direction.

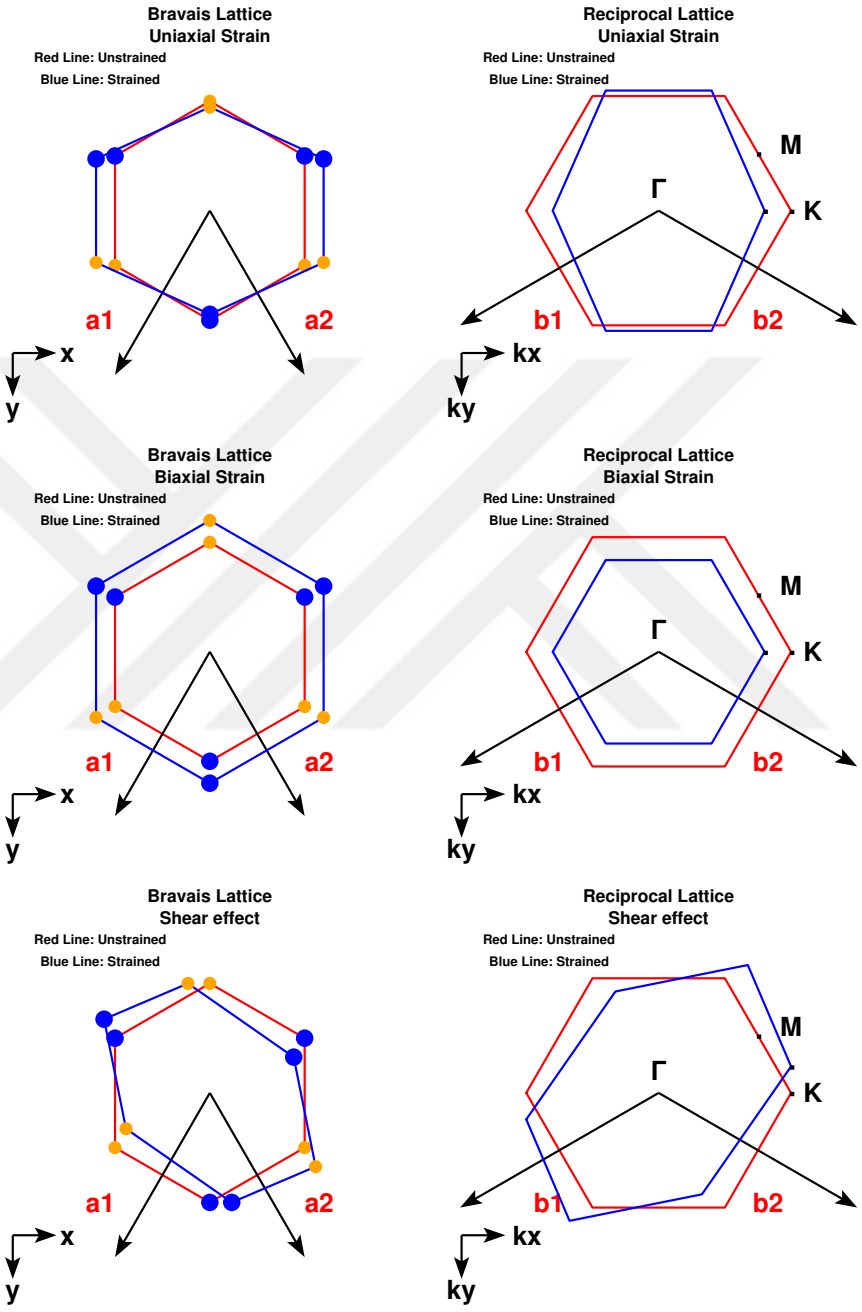

Figure 2.4: Schematic of lattice deformation of the TMDs in reciprocal space under uniaxial and biaxial strain as well as shear effect.

2.3 Strain Dependance of Excitonic Effective Mass and Electronic Band Gap of TMDs

Band gap energy for different TMDs under various types of applied strain is plotted in Fig. 2.5 from Eq. 2.10. Fig. 2.6 and Fig. 2.7 show the effect of uniaxial and biaxial strain on exciton's effective mass of different TMDs in both x and y direction, respectively. As it can be seen from these figures, for uniaxial and biaxial strain μ_{xx} equals to μ_{yy}. Quantitatively the implicit electron-hole symmetry from Eq. 2.16 equates effective masses in both directions. For shear strain, there is no change in both the band gap and the effective mass for both directions.

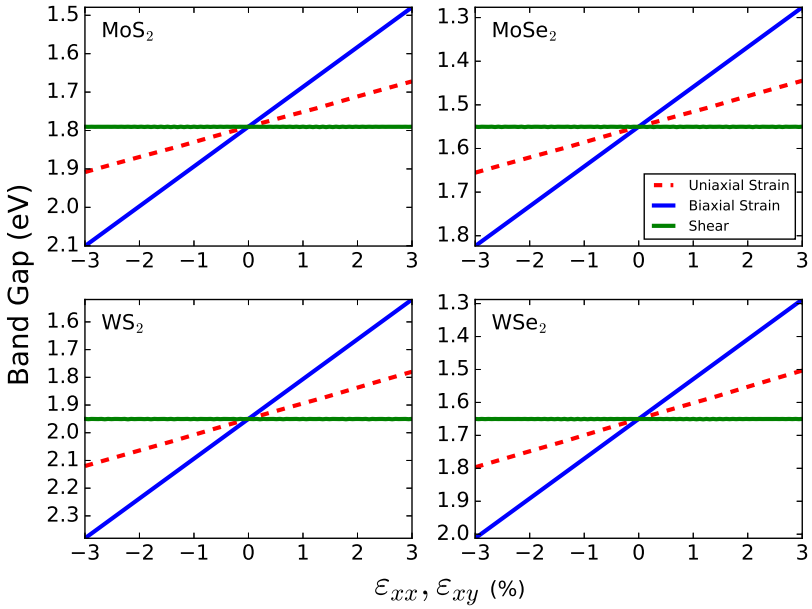

Figure 2.5: Effects of uniaxial strain (Red-dashed), biaxial strain (Blue-solid) and shear effect (Green-solid) on band gap energy of different TMDs.

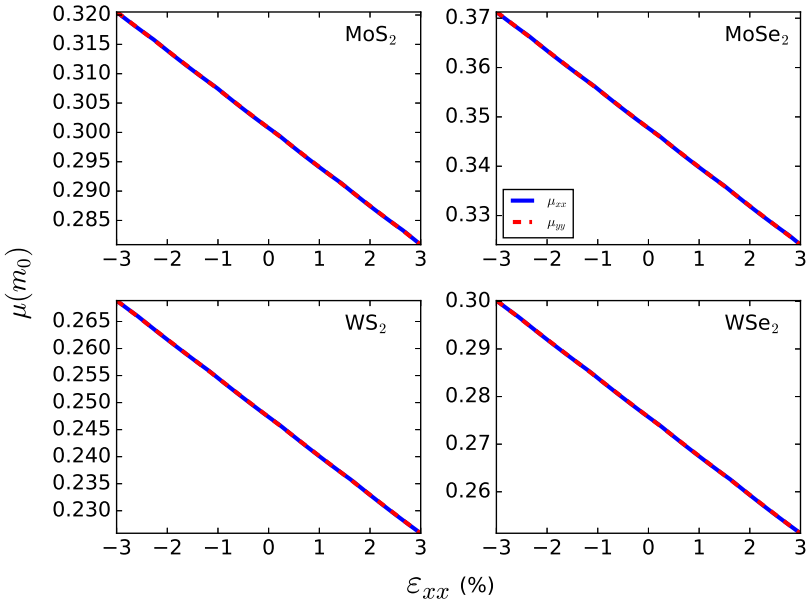

Figure 2.6: Effects of uniaxial strain on effective mass for different TMDs in x direction (Blue-solid) and y direction (Red-dashed).

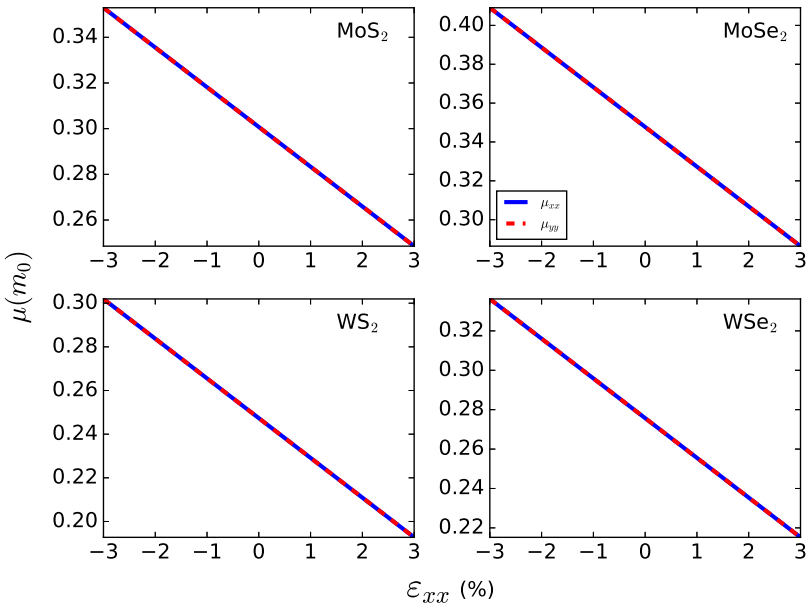

Figure 2.7: Effects of biaxial strain on effective mass for different TMDs in x direction (Blue-solid) and y direction (Red-dashed).

Chapter 3

Strain Dependence of Photoluminescence and Circular Dichroism in TMDs

TMDs retain direct optical gap along with mechanical flexibility up to 10% range [77] which permits broad strain tunability of their optoelectronic properties [78, 75]. Within a short time span several groups have been demonstrated that the electronic structure of monolayer MoS_2 can be tuned by applying a uniaxial tensile to the underlying flexible substrates [9, 12, 5, 14, 79, 15, 80]. The continuous and reversible tuning of the optical bandgap over an ultralarge range of applied biaxial strain is demonstrated by Lloyd et al. for a suspended monolayer MoS_2 membrane [13]. Sec. 3.1 of this chapter discusses the circular dichroism (CD) in TMDs that refers to the helicity-selective optical absorption [81] and in which way it can be altered by strain. In Sec. 3.2 calculation method is given for exciton and trion binding energies to be utilized in the subsequent section. Sec. 3.3 provides experimental photoluminescence (PL) data on strained TMD samples in support of a simple two-band $k \cdot p$ theory. Analysis and results in this Chapter are already published in Ref. [82].

3.1 Strain Effect on Circular Dichroism

The dipole matrix element connecting valence $|U_v\rangle$ and conduction $|U_c\rangle$ states for a polarized light along a unit vector $\hat{u}$ is given by [83]

$$\mathcal{P}_u(\vec{k}) \equiv \frac{m_0}{\hbar} \langle U_c| \frac{\partial \hat{H}}{\partial k_u} |U_v\rangle \ , \tag{3.1}$$

where m_0 is the free electron mass. For the $\pm$ circularly polarized light defined by the unit vectors $\hat{u}_\pm = (\hat{x} \pm i\hat{y})/\sqrt{2}$,

$$\hat{\mathcal{P}}_\pm = \hat{\varepsilon_\pm}.\hat{\vec{p}} = \frac{1}{\sqrt{2}} \left(\hat{\mathcal{P}}_x \pm i\hat{\mathcal{P}}_y \right) = \frac{m_0}{\sqrt{2}\hbar} \left(\frac{\partial \hat{H}}{\partial k_x} \pm i \frac{\partial \hat{H}}{\partial k_y} \right). \tag{3.2}$$

From Eq. 2.3, $\frac{\partial \hat{H}}{\partial k_x} = f_2 a \hat{\sigma_x}$, $\frac{\partial \hat{H}}{\partial k_y} = f_2 a \hat{\sigma_y}$. Thus, Eq. (3.2) in terms of Pauli spin raising/lowering operators $\hat{\sigma}_\pm$ is given as

$$\mathcal{P}_\pm(\vec{k}) = \frac{m_0 f_2 a}{\sqrt{2}\hbar} (\hat{\sigma_x} \pm i\hat{\sigma_y}) = \frac{m_0 f_2 a}{\sqrt{2}\hbar} \langle U_c|\hat{\sigma}_\pm|U_v\rangle \, . \tag{3.3}$$

This quantity has a use in $k-$resolved degree of optical polarization which is defined as [81],

$$\eta(\vec{k}) \equiv \frac{|\mathcal{P}_+(\vec{k})|^2 - |\mathcal{P}_-(\vec{k})|^2}{|\mathcal{P}_+(\vec{k})|^2 + |\mathcal{P}_-(\vec{k})|^2} \, . \tag{3.4}$$

For isotropic and electron-hole symmetric bands, $\eta(\vec{k}) \to \eta(E)$. Thus, excess energy ΔE can be simply considered from the band minima. Inserting the associated states from Eq. (2.13) a simple analytical form comes out as,

$$\eta(q, \varepsilon_H) = \frac{1 - [r(q, \varepsilon_H)]^4}{1 + [r(q, \varepsilon_H)]^4}, \tag{3.5}$$

in terms of $r(q, \varepsilon_H)$ as defined in Eq. (2.12).

To explain how strain impacts this situation, we plot $\eta(\Delta E)$ using Eq. (3.4) in Fig. 3.1 for different excess energies defined as $\Delta E = (E - E_g)/2$, which E is the energy of the incoming photon. For the nature of uniaxial and biaxial strain with $\varepsilon_H \neq 0$, the existance of a hydrostatic strain component ε_H either increases or decreases the alternation in the mixing function r and hence η depending on the overall sign of $f_4\varepsilon_H$. With $f_4 < 0$ as it can be seen from Table 2.1, this clarifies

why the tensile strain $\varepsilon_H > 0$ ($\varepsilon_{xx} > 0$ in Fig. 3.1) inflates the change in η in Fig. 3.1. Also, it is observed that selenium-TMDs are more sensitive to strain in this respect, and for biaxial strain the amount of variation is larger than uniaxial case for all of these materials. For shear strain $\varepsilon_H = 0$. Hence, as it is shown in Fig. 3.1 the total amount of η would remain constant for all amounts of applied shear.

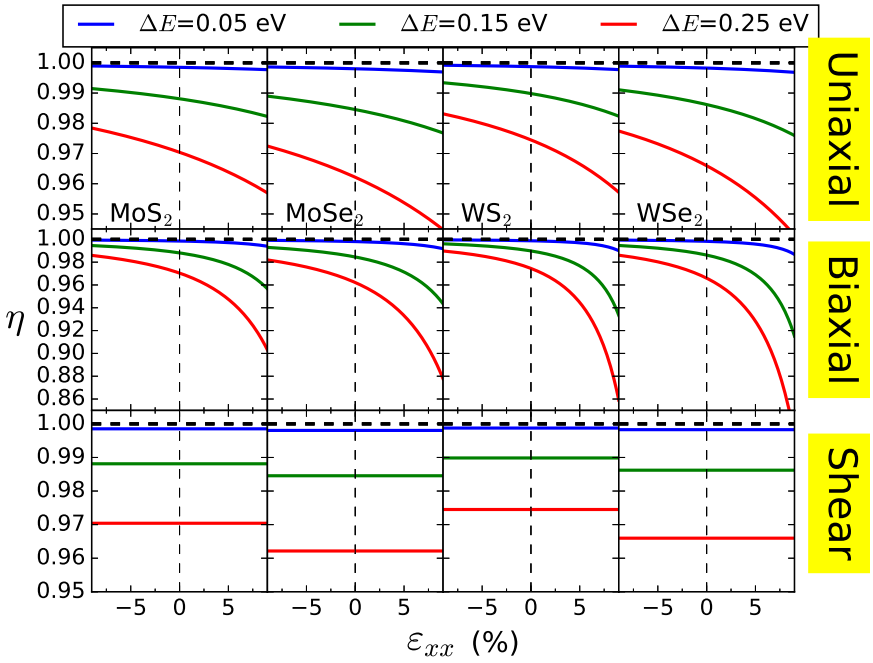

Figure 3.1: Different strain types effect on the degree of optical polarization of TMDs for two compressive and tensile strain. Excess energies ΔE are measured from the conduction band minimum.

3.2 Calculations of Neutral Exciton and Charged Exciton (Trion) Binding Energies

To compare with the experimental PL data under a given strain, we need to include excitonic effects as the associated binding energies significantly exceed the thermal energy at room temperature [12]. The binding energies for neutral

and charged excitons (trions) in TMDs can be calculated by a variational method based on the exciton Hamiltonian [67] (switching to Hartree atomic units in the remainder of this chapter). Within the effective mass approximation from sec. 2.1 exciton-Hamiltonian would be defined as,

$$\mathcal{H}_X = \frac{\nabla_\rho^2}{2\mu} - V_{2D}(\rho) \tag{3.6}$$

and trion-Hamiltonian as

$$\mathcal{H}_{X^-} = -\frac{1}{2\mu}(\nabla_{\rho_1}^2+\nabla_{\rho_2}^2) - \frac{1}{2m_h}\nabla_{\rho_1}.\nabla_{\rho_2} - V_{2D}(\rho_1) - V_{2D}(\rho_2) + V_{2D}(|\rho_1+\rho_2|), \tag{3.7}$$

where, the effective in-plane 2D interaction for charges separated by $\rho = \sqrt{x^2+y^2}$ comes from,

$$V_{2D}(\rho) = \frac{\pi e^2}{(\varepsilon_1+\varepsilon_2)\rho_0}\left[H_0(\rho/\rho_0) - Y_0(\rho/\rho_0)\right], \tag{3.8}$$

where H_0 and Y_0 are the Struve function and the Bessel function of the second kind. Screening length is given by $\rho_0 = 2\pi\chi_{2D}$ which χ_{2D} is the 2D polarizability of the planar material [84].

The variational wave function for free exciton is chosen as,

$$\Psi_X(\rho; a) = \sqrt{\frac{2}{\pi a^2}}\exp\left(-\rho/a\right), \tag{3.9}$$

and for trions it is given as a symmetrizing product of exciton wave functions such that,

$$\Psi_{X^-}(\rho_1;\rho_2;a;b) = 2^{-1/2}[\Psi_X(\rho_1;a)\Psi_X(\rho_2;b) + \Psi_X(\rho_2;a)\Psi_X(\rho_1;b)]. \tag{3.10}$$

Here a and b are the variational parameters. Kinetic energy as well as potential energy for free exciton can be calculated from Eq. 3.6 along with Eq. 3.9. The result for kinetic energy can be evaluated analytically as,

$$T(a) = 1/2\mu a^2, \tag{3.11}$$

while potential energy requires a numerical integration that is obtained after some analytical simplifications,

$$V(a) = -\frac{2\pi}{\rho_0 a^2}\int_0^\infty \left[H_0(\rho/\rho_0) - Y_0(\rho/\rho_0)\right]\ \exp\left(-2\rho/a\right)\ \rho\ d\rho. \tag{3.12}$$

Exciton binding energy can be found by minimizing $E_X = T(a) + V(a)$, where the optimum value of a is an estimate of the exciton radius.

In the same way, Eq. 3.7 in combination with Eq. 3.10, gives kinetic-energy (analytically) and potential energy (numerically) of charged excitons (trions) as below,

$$T(a,b) = \frac{1}{\mu(ab)^2}[\frac{a^2+b^2}{2} + \frac{16}{ab(1/\rho_1 + 1/\rho_2)^4}], \tag{3.13}$$

The final form for the potential energy comes out as below that then can be computed numerically,

$$\begin{aligned}
V(a,b) = &-\frac{4\pi}{\rho_0(ab)^2}\Bigg[\frac{b^2}{4}\int_0^\infty (H_0(\rho_1/\rho_0) - Y_0(\rho_1/\rho_0))\exp(-2\rho_1/a)\rho_1 d\rho_1 \\
&+ \frac{2}{(1/a+1/b)^2}\int_0^\infty (H_0(\rho_1/\rho_0) - Y_0(\rho_1/\rho_0))\exp(-\rho_1(1/a+1/b))\rho_1 d\rho_1 \\
&+ \frac{a^2}{4}\int_0^\infty (H_0(\rho_1/\rho_0) - Y_0(\rho_1/\rho_0))\exp(-2\rho_1/b)\rho_1\ d\rho_1\Bigg] \\
&- \frac{4\pi}{\rho_0(ab)^2}\Bigg[\frac{b^2}{4}\int_0^\infty (H_0(\rho_2/\rho_0) - Y_0(\rho_2/\rho_0))\exp(-2\rho_2/a)\rho_2 d\rho_2 \\
&+ \frac{2}{(1/a+1/b)^2}\int_0^\infty (H_0(\rho_2/\rho_0) - Y_0(\rho_2/\rho_0))\exp(-\rho_2(1/a+1/b))\rho_2\ d\rho_2 \\
&+ \frac{a^2}{4}\int_0^\infty (H_0(\rho_2/\rho_0) - Y_0(\rho_2/\rho_0))\exp(-2\rho_2/b)\rho_2 d\rho_2\Bigg] \\
&+ \frac{4}{\rho_0(ab)^2}\Bigg[\int_0^\pi\int_0^\infty\int_0^\infty (H_0(\frac{\sqrt{\rho_1^2+\rho_2^2-2\rho_1\rho_2 cos(2\phi)}}{\rho_0}) \\
&- Y_0(\frac{\sqrt{\rho_1^2+\rho_2^2-2\rho_1\rho_2 cos(2\phi)}}{\rho_0}))\exp(-2\rho_1/a)\exp(-2\rho_2/b)\rho_1\rho_2 d\rho_1 d\rho_2 d\phi \\
&+ 2\int_0^\pi\int_0^\infty\int_0^\infty (H_0(\frac{\sqrt{\rho_1^2+\rho_2^2-2\rho_1\rho_2 cos(2\phi)}}{\rho_0}) \\
&- Y_0(\frac{\sqrt{\rho_1^2+\rho_2^2-2\rho_1\rho_2 cos(2\phi)}}{\rho_0}))\exp(-\rho_1(1/a+1/b))\exp(-\rho_2(1/a+1/b)) \\
&\rho_1\rho_2 d\rho_1 d\rho_2 d\phi \\
&+ \int_0^\pi\int_0^\infty\int_0^\infty (H_0(\frac{\sqrt{\rho_1^2+\rho_2^2-2\rho_1\rho_2 cos(2\phi)}}{\rho_0}) \\
&- Y_0(\frac{\sqrt{\rho_1^2+\rho_2^2-2\rho_1\rho_2 cos(2\phi)}}{\rho_0}))\exp(-2\rho_1/b)\exp(-2\rho_2/a)\rho_1\rho_2 d\rho_1 d\rho_2 d\phi\Bigg].
\end{aligned} \tag{3.14}$$

Minimizing the $T(a,b) + V(a,b)$ would give us the total mechanical energy for trions. Here, the differing exciton radii, $a \neq b$, essentially allows one electron to sit close to the hole, near the neutral exciton radius, while the other is further away to minimize the unfavorable electron-electron repulsion. Finally, subtracting this trion mechanical energy from that of free excitons (E_x) gives trion binding energy.

3.3 PL Peak Shift Under Strain

Figure 3.2 comparies the PL peak shift for the four TMDs under uniaxial strain from our calculations with the data from numerous experimental references. There is a good agreement between our theory and the best fit to the experimental data for MoS_2 and WSe_2, taking into account the spread in the latter. Unlike these, our results are in disagreement with two Refs. [19, 85] for WS_2. To illuminate this . we also plot the bandgap shift under uniaxial strain from a first-principles calculation [36] (yellow-dashed). By adding the strained excitonic correction to this, a closer agreement comes out with our calculations (purple-dotted vs. blue-solid). Considering that the TMDs are clamped to the substrate by different methods in all other measurements of Fig. 3.2 such as Refs. [12, 21, 22], we believe that some slipping may have occured on the TMD layer while applying strain to the substrate in Refs. [19, 85]. Finally, the uniaxial *stress* condition for $MoSe_2$ matches perfectly with the data, using the Poisson's ratio of the substrate, $\nu = 0.37$ (blue-dashed) which is in agreement with their assertion in Ref. [22]. In other words, for this experiment the TMD layer fully satisfies the Poisson's contraction of the substrate, as opposed to the other measurements in Fig. 3.2.

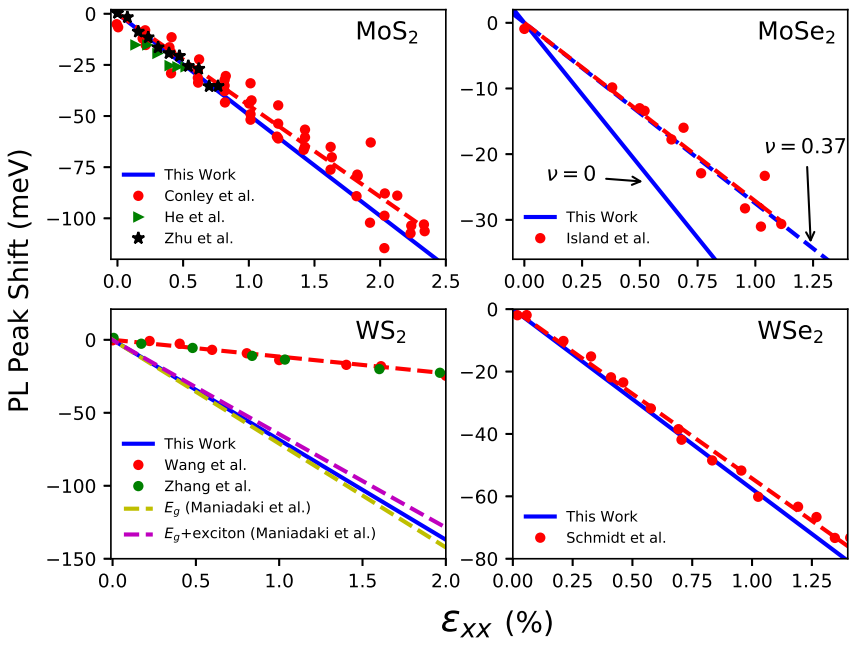

Figure 3.2: *A*-exciton PL peak energy shift under uniaxial strain for monolayer TMDs. Our calculations (in blue) is compared to experimental data (symbols). Red-dashed line is the best fit to the experimental data. References: Conley *et al.* [12], He *et al.* [9], Zhu *et al.* [5], Island *et al.* [22], Wang *et al.* [19], Zhang *et al.* [85], Schmidt *et al.* [21], Maniadaki *et al.* [36].

Fig. 3.3 displays the same comparison for the case of biaxial strain. For MoS_2 there is an excellent agreement with the widest-range strain data by Lloyd *et al.* [13] which lies up to 6%. green-dashed in upper-left panel shows the variation in the bandgap; the notable offset from PL line demonstrates the extend of excitonic input on the strain variation of the PL energy. Here, Ref. [13] as well as our result are for freestanding monolayer TMDs. The remaining biaxial strain data from Ref. [86] was reported with respect to polypropylene substrate strain. Therefore, we multiplied all strain data from this reference by the 0.573 scale factor to convert substrate strain results in Ref. [86]. This matches their data with the freestanding case of Ref. [13]. However, for $MoSe_2$ still a disagreement is seen with Ref. [86]; we again suspect that a slipping might be responsible, noting the leveling off in their data beyond about 0.15% strain.

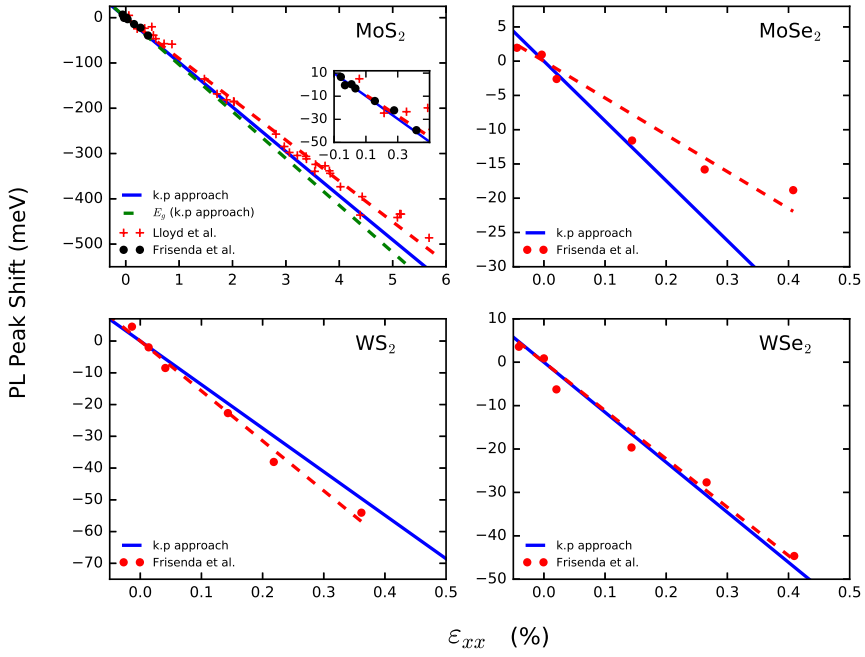

Figure 3.3: *A*-exciton PL peak energy shift under Biaxial strain for monolayer TMDs. Our calculations (in blue) is compared to experimental data (symbols). Red-dashed line is the best fit to the experimental data. References: Lloyd *et al.* [13], Frisenda *et al.* [86].

Table 3.1 gives a comparison in between our PL peak strain shift results with the quantities from different experimental references. For our results, both uniaxial strain and uniaxial *stress* cases are presented. In the former no transverse contraction occurs in the direction perpendicular to axial deformation (i.e., $\nu = 0$). For uniaxial stress we use $\nu = 0.37$ value, typical for the flexible substrates in use [21, 22]. Note that the uniaxial stress condition applies only for the $MoSe_2$ experiment of Ref. [22]. Our results excluding the variation of exciton binding energy under strain is given in parentheses. It can be observed that sulfur-TMDs are more receptive to strain for PL peak shift. Also, for each material considered the amount of change for biaxial strain is larger than the uniaxial one.

Table 3.1: PL peak redshift under uniaxial or biaxial strain in comparison with results from literature. Our results (this work) have both uniaxial strain/stress (i.e., ν =0/0.37) cases with the values in parentheses corresponding those without the excitonic contribution.Uniaxial or biaxial strain PL peak shift along with results from literature. Our results (this work) is given for both uniaxial strain/stress (i.e., ν =0/0.37) cases. The values in parentheses gives those without the excitonic contribution.

meV/%	MoS_2		$MoSe_2$		WS_2		WSe_2	
	Uniaxial	Biaxial	Uniaxial	Biaxial	Uniaxial	Biaxial	Uniaxial	Biaxial
This Work	49.4/31.1 (51.8/32.6)	98.8 (103.6)	43.6/27.5 (45.6/28.7)	87.2 (91.2)	68.5/43.2 (71.8/45.2)	137 (143.6)	57.6/36.3 (60.4/38.1)	115.2 (120.8)
Literature	∼45[a], ∼70[b], ∼48[c]	99±6[d], (90.15), 90.1[e]	27±2[f]	53.74[e]	11.3[g], 10[h]	157[e]	54[i]	111[e]

[a] Ref. [12], [b] Ref. [9], [c] Ref. [5], [d] Ref. [13], [e] Ref. [86], [f] Ref. [22], [g] Ref. [19], [h] Ref. [85], [i] Ref. [21]

Chapter 4

Strain Dependence of CD for a Monolayer MoS_2 via an Effective $k \cdot p$ Analysis

In both previous chapters we used an effective 2 band-$k \cdot p$ Hamiltonian to describe TMDs and the effect of strain on these monolayer materials [87]. Even though this Hamiltonian describes well the TMD structures around K valley, it is isotropic and preserves electron-hole symmetry regarding the valence and conduction bands. Also, trigonal warping (TW) of the isoenergy counters, in the immediate vicinity of K point is absent in this model. Electron-hole symmetry breaking has been confirmed by magnetoluminescence experiments recently [88, 89]. Zhang et al. argued that TW leads to measurable effects in the polarization of electroluminescence in pn junctions [90]. To discuss these experimental observations Kormányos et al. argue that the TW of the bands can be understood as a consequence of the coupling of the valence band (VB) and conduction band (CB) to other (remote) bands and describe by a four-band generalized bilayer-graphene-type Hamiltonian [66]. Later, they derive an effective two-band model from this four-band model using the Löwdin partitioning [91]. Sec. 4.1 contains the details of their model. The effects of electron-hole asymmetry as well as TW

effect on energy dispersion, CB/VB effective mass and CD of an unstrained monolayer MoS_2 are explained in Sec. 4.2, Sec. 4.3 and Sec. 4.4 respectively. Sec. 4.5 argues about the effect of uni/biaxial strain on CD for a monolayer MoS_2, and takes electron-hole asymmetry and TW effect into account.

4.1 Effective 2 Band-$k \cdot p$ Approach in TMDs Including Electron-Hole Symmetry Breaking and Trigonal Warping Effect

2 band-$k \cdot p$ Hamiltonian for TMDs is given in Ref. [87] as,

$$H_0 = \frac{f_1}{2}\hat{\sigma}_z + f_2 a(k_x\hat{\sigma}_x + k_y\hat{\sigma}_y). \tag{4.1}$$

The effects of strain is discussed by counting strain Hamiltonian to H_0 as,

$$H = H_0 + H_{strain}, \tag{4.2}$$

where H_{strain} is defined as [87],

$$H_{strain} = f_4(\varepsilon_{xx} + \varepsilon_{yy})\hat{\sigma}_z + f_5\big[(\varepsilon_{xx} - \varepsilon_{yy})\hat{\sigma}_x - 2\varepsilon_{xy}\hat{\sigma}_y\big] \tag{4.3}$$

In both Hamiltonians, f_i's are $k \cdot p$ parameters for different TMD materials, a is the lattice constant and σ_α's are Pauli matrices. Here, we drop the constant midgap position parameters f_0 and f_3 in Ref. [87]. They can be incorporated in the study of heterostructures for their proper band alignment. Effective 2 band $k \cdot p$ Hamiltonian constructed by Kormányos et al. [66] considering Eq. 4.2 is given by,

$$H_{2B} = H_0 + H_{strain} + H_{as} + H_{TW} + H_{cub}, \tag{4.4}$$

$$H_{as} = \begin{pmatrix} \beta k^2 & 0 \\ 0 & \alpha k^2 \end{pmatrix}, \tag{4.5}$$

$$H_{TW} = \kappa \begin{pmatrix} 0 & k_+^2 \\ k_-^2 & 0 \end{pmatrix}, \tag{4.6}$$

$$H_{cub} = \frac{\eta}{2} k^2 \begin{pmatrix} 0 & k_- \\ k_+ & 0 \end{pmatrix}, \tag{4.7}$$

with the notation in which K_+ valley is set as origin for k wavevector and $k_\pm = k_x \pm i k_y$. α and β describe the electron-hole symmetry breaking, whereas κ is responsible for the TW of the energy contours. H_{cub} is important to achieve a quantitative fit to the VB away from the K point [66].

4.2 Energy Dispersion of a Monolayer MoS_2 Around K Valley

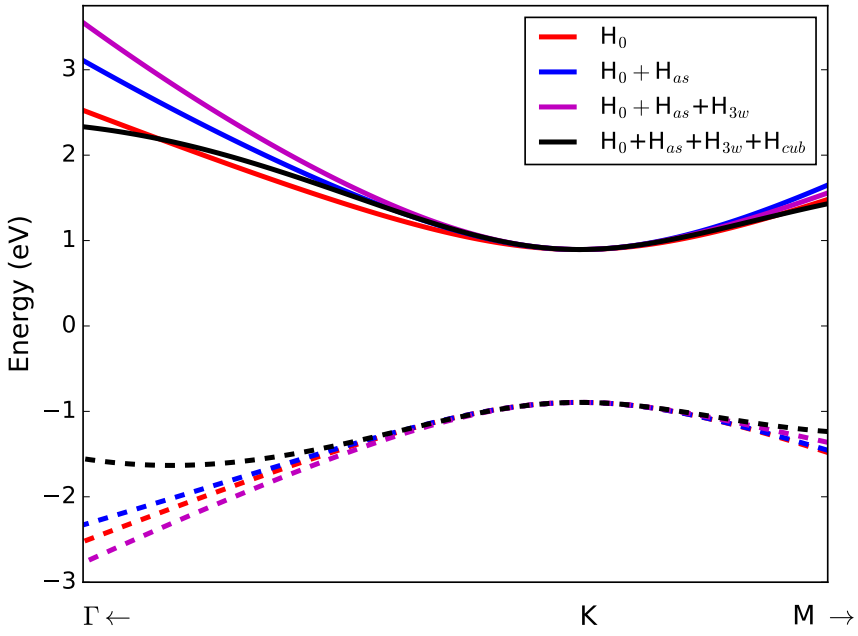

Figure 4.1: Dispersion curve for 2D MoS_2 around K valley with various Hamiltonians.

We plot the energy dispersion curve for conduction and valence bands of an unstrained MoS_2 around K valley with the effective Hamiltonian discussed above in Fig. 4.1. Here, we use the parameters $\alpha = 1.72$ eVÅ^2, $\beta = -0.13$ eVÅ^2,

$\kappa = -1.02$ eVÅ^2, $\eta = 8.52$ eVÅ^3 from Ref. [66] and $f_1 = 1.79$ eV, $f_2 = 1.06$ eV, $a = 3.182$ Å from Ref. [64]. As it can be seen from this figure, for H_0 conduction and valence bands (solid and dashed red lines) are symmetric. Adding H_{as} to this initial Hamiltonian which is responsible for electron hole asymmetry, creates blue solid (dashed) line for conduction (valence) band. Here, symmetry breaking of the band structure is obvious. Purple lines include effects of electron-hole asymmetry as well as trigonal warping into the band structure. In black lines H_{cub} is included as well. Here, quantitative fit to the bands are clear.

4.3 Effective Mass of Conduction and Valence Band for a Monolayer MoS_2

Table 4.1: Conduction and valence bands effective mass for a monolayer MoS_2

MoS_2	Ref. [66]	Eq. 4.4
m^{c}_{eff}/m_0	0.48	0.47
m^{v}_{eff}/m_0	-0.62	-0.59

We calculate the effective mass for conduction and valence bands using the same parameter as is given in previous section. Table. 4.1 lists results from our calculations along with the quantities from Ref [66]. Both are in close agreement with each other. The effective mass is different for conduction and valence bands which confirms the electron-hole symmetry breaking.

4.4 Circular Dichroism of MoS_2

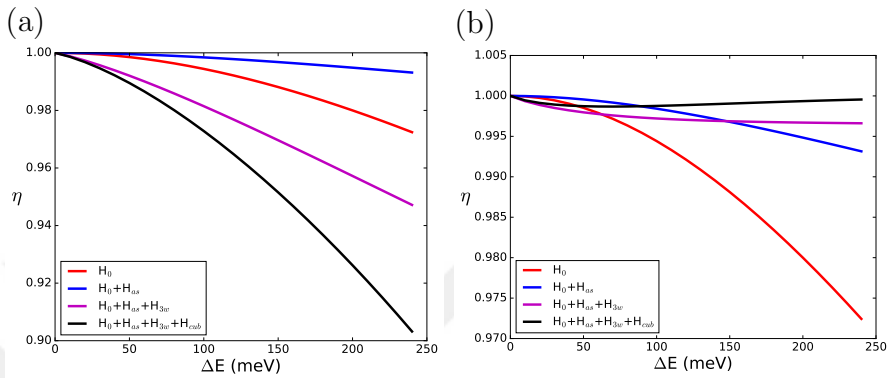

Figure 4.2: Circular dichroism for a monolayer MoS_2 in respect to the excess amount of energies for a k value from (a) $(M-K)$ and (b) $(\Gamma-K)$ intervals. Different colors corresponds to quantities from different Hamiltonians.

$k-$resolved degree of optical polarization can be defined by Eqs. 3.4 and 3.2 for any Hamiltonian. In order to show how electron-hole asymmetry and trigonal warping affects the CD, we plot $\eta(k)$ by including different Hamiltonian terms from Eqs. 4.5−4.7 in Eq. 4.1 for excess amount of energy defines as $\Delta E = E - E_g$. We used the conduction band to calculate ΔE and its wavevector $(k_{x/y})$ as a point to find CD there. As the band structure is not symmetric anymore, there would be two different k quantities from $K-\Gamma$ and $M-K$ intervals for a given ΔE. Fig. 4.2 shows the circular dichroism with respect to excess energies for k value from (a) $(M-K)$ and (b) $(\Gamma-K)$ intervals. When k is coming from $M-K$ interval (Fig. 4.2 (a)), for an isotropic Hamiltonian H_0 (red line) the amount of CD is decreasing by increasing of the energy difference from the minimum energy of conduction band (ΔE). Adding H_{as} to the isotropic term (blue line), decreases the amount of suppression from $\eta = 1$ by increasing number of ΔE. Both H_{3w} and H_{cub} terms have increasing effect on the suppression amount of η. For a k from $\Gamma - K$ interval (Fig. 4.2 (b)), results from H_0 and $H_0 + H_{as}$ are the same as the previous results. Taking trigonal warping effect into account does not change CD quantity from its initial value $(\eta = 1)$ appreciably. Inclusion of cubic term to

the Hamiltonian suppresses this change of CD even more.

4.5 Strain Dependance of CD in Monolayer MoS_2

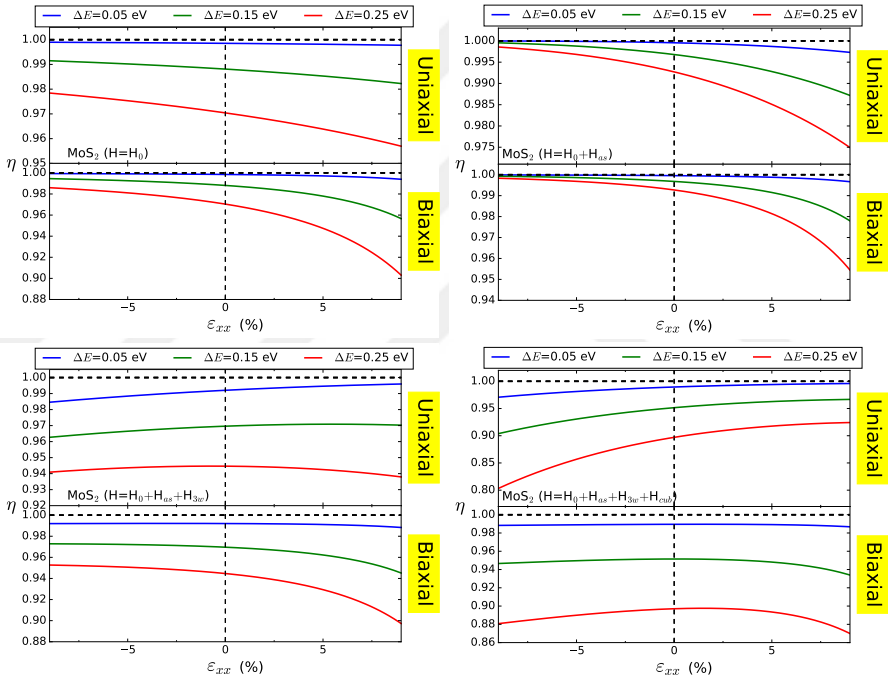

Figure 4.3: Different strain types effect on the degree of optical polarization of a monolyer MoS_2 for two compressive and tensile strain. Excess energies ΔE are measured from the conduction band minimum. Here, k is from $K-M$ interval

In this section we discuss the effects of strain on the CD by taking into account the electron-hole asymmetry as well as trigonal warping and cubic term effects. Figs. 4.3 and 4.4 show the effect of uniaxial/biaxial strain on the degree of optical polarization of a monolayer MoS_2 for compressive/tensile strain at different excess energies ΔE, as measured from the conduction band minimum. Fig. 4.3 correspond to a k from $K-M$ interval and Fig. 4.4 correspond to a k from $\Gamma-K$ interval. As it can be seen from the figures for a k from $K-M$ interval the

amount of change in CD quantity is more than this amount for the k from $\Gamma - K$ interval.

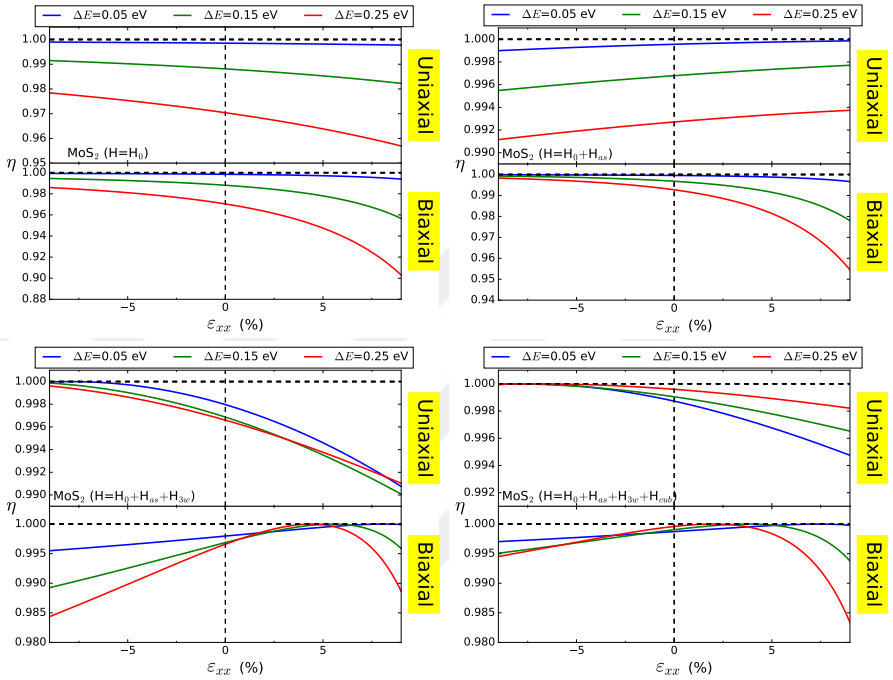

Figure 4.4: Different strain types effect on the degree of optical polarization of a monolyer MoS_2 for two compressive and tensile strain. Excess energies ΔE are measured from the conduction band minimum. Here, k is from $\Gamma - K$ interval.

Chapter 5

Strain Dependence of Berry Curvature and Orbital Magnetic Moment in a Monolayer WSe_2

TMDs have distinct K and $-K$ valleys at the corners of hexagonal Brillouin zone. This energy degeneracy in momentum space, provides a quantum degree of freedom for electrons as valley pseudospin. Theoretical studies were predicted for physical properties like valley Hall effect [62] and valley-dependent optical selection rules [92] inside TMDs due to the broken inversion symmetry. Furthermore, strong spin-orbit coupling (SOC) along with the broken inversion symmetry expected possible control of spin and valley in these materials [93]. In pursuit of these explorations many theoretical [94, 95] and experimental [96, 97, 98, 99, 90, 100, 101, 102] studies have been done recently in the field of valleytronics.

Berry curvature ($\boldsymbol{\Omega}$) and orbital magnetic moment ($\boldsymbol{m}$) are two main quantities to manipulate valley pseudospin in TMDs. $\boldsymbol{\Omega}$ generates an anomalous velocity perpendicular to the applied electric field. Thus, electrons in each valley flow in opposite direction. The so called valley Hall effect and the consequent investigation have been conducted recently in TMDs [103, 93, 104, 105]. $\boldsymbol{m}$ is related

to the self-rotating action of electrons that makes energy-control possible with an applied magnetic field [60, 89, 88, 55]. Based on all these explanations, the modification of these two physical magnitudes has essential role in the progressive research. Here, we investigate the deterministic effect of strain on $\mathbf{\Omega}$ theoretically. To do so, first a new $k \cdot p$ parameter set is given for four different TMD materials in Sec. 5.1 and Sec. 5.2. Later, strain incorporated to an available three-band tight-binding (TB) Hamiltonian in Sec. 5.3. Berry curvature and orbital magnetic moment are compared in Sec. 5.4 from both developed $k \cdot p$ method and TB model. Finally, the effect of strain on these two parameters is given in Sec. 5.5. All figures and tables of this Chapter is already published in Ref. [106].

5.1 Fitting Procedure and Data References for Different TMDs

Table 5.1: $k \cdot p$ parameters. a is Lattice constant [107], E_g i single-particle band gap [108], $\bar{\Omega}$ is average of BC [109], $m^*_{\rm vb}$ ($m^*_{\rm cb}$) is VB (CB) effective mass[110]. E_g, and the two-band $k \cdot p$ parameters are based on lowest spin-allowed VB-CB transition between spin-down ($\downarrow$) states [110].

Materials	MoS_2	$MoSe_2$	WS_2	WSe_2
a (Å)	3.190	3.326	3.191	3.325
$E_{\rm gap}$ (eV)	2.15	2.18	2.38	2.20
$\lvert\bar{\Omega}\rvert$ (Å^2)	10.43	10.71	16.03	17.29
$m^*_{\rm vb,\downarrow}$ (m_0)	-0.54	-0.59	-0.35	-0.36
$m^*_{\rm cb,\downarrow}$ (m_0)	0.43	0.49	0.26	0.28
$m^*_{\rm vb,\uparrow}$ (m_0)	-0.61	-0.7	-0.49	-0.54
$m^*_{\rm cb,\uparrow}$ (m_0)	0.46	0.56	0.35	0.39

Our discussed model depends on the following nine parameters:
a, f_1, f_2, f_4, f_5, α, β, κ, η . In this section we describe how to find all these

parameters. a is lattice constant for different TMDs where we use GGA/DFT model calculations from Ref. [107] (Table. 5.1). f_1 corresponds to the free particle band gap without excitonic contributions. Experimental data is listed in the recent review Ref. [108] for this parameter (Table. 5.1). Berry curvature equation at K valley can be calculated as $\Omega(K) = \pm 2(f_2/f_1)^2$ [62]. The average of this quantity for the lowest spin-allowed transitions in K valley ($\bar{\Omega} = \frac{(|\Omega_{\mathrm{CBM}}|+|\Omega_{\mathrm{VBM}}|)}{2}$) is fitted to the results from first principle calculation model in Ref. [109] (Table. 5.1) to find f_2 parameter. f_4 and f_5 parameters come from Ref. [87] without any change. After these set of parameters for H_0, we go through α and β from H_{as}. To find these two parameters we fit calculated effective mass quantities from Eq. 4.1+Eq. 4.5 to these quantities from Ref. [110] (Table. 5.1). Here, we deal with effective mass of lowest spin-allowed transitions in the fitting procedure.

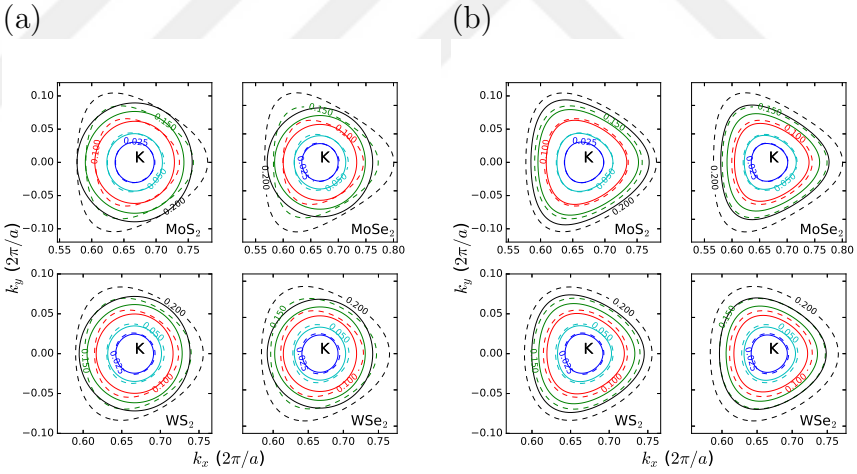

Figure 5.1: Isoenergy contours of the VB (eV) for different TMDs. Dashed line is from TB and solid line is from $k \cdot p$ model. The latter exludes (a), or includes (b) the TW effect.

Fig. 5.1 (a) shows isoenergy contours plotted using Eq. 4.1+Eq. 4.5 (solid lines) and from (Third Nearest Neighber) TNN TB model calculations of Ref. [107] (dashed lines). Each color corresponds to different excess amount of energies from valence band maximum. As it can be seen from this figure TW effect is absent in $k \cdot p$ calculations as all curves are circular. By adding Eq. 4.6 to the

previous Hamiltonian (Eq. 4.1+Eq. 4.5) *TW* effect on the isoenergy contours emerges (Fig. 5.1 (b)). Here we find κ parameter by fitting the isoenergy contour plot of $k \cdot p$ model to the TNN TB model in 100 meV excess amount of energy. Finally to find η parameter we fit the band structure of different TMDs calculated from Eq. 4.4 to the recent DFT model calculation results.

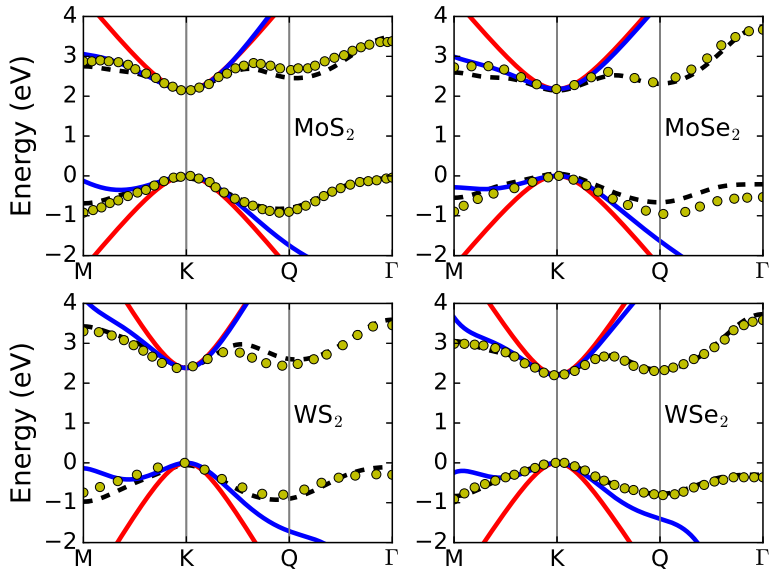

Figure 5.2: $k{\cdot}p$ band structure of monolayer TMDs. Blue (Red) line includes (does not include) electron-hole symmetry breaking, TW and nonparabolic effects. This result compared with the TB calculations which is shown with black dashed lines, and DFT results collected from various references (yellow dots). VB maxima are set to zero energy, and the band gaps is corrected to the values in Table. 5.1 in each case.

Table 5.2: $k \cdot p$ fitted parameters and the amount of agreement in energy for conduction and valence bands.

Materials	MoS_2	$MoSe_2$	WS_2	WSe_2
f_1 (eV)	2.15	2.18	2.38	2.2
f_2 (eV)	1.54	1.52	2.11	1.95
f_4 (eV)	-2.59	-2.28	-3.59	-3.02
f_5 (eV)	2.2	1.84	2.27	2.03
α (eV·Å^2)	4.16	5.22	8.2	8.43
β (eV·Å^2)	-2.35	-3.9	-4.43	-5.4
κ (eV·Å^2)	-1.9	-1.8	-2.2	-2
η (eV·Å^3)	6	8	14	18
VB Fit Range (meV)	350	400	200	100
CB Fit Range (meV)	115	170	70	90

Fig. 5.2 shows band structure of different TMDs from Eq. 4.1 in ustrained case (red curves) and Eq. 4.4 with our $k \cdot p$ fitted parameters (blue curves) along with data from DFT model calculations (yellow dots). All fitted parameters for DFT calculation results in each TMD material is given in Table. 5.2. Furthermore, we plot band structures from TNN TB model [107] (black dashed curves) in this figure to observe how precise is our model. Here, DFT and TNN TB model calculation agreements is pronounced. Also, the blue curves gets closer to DFT and TB model calculation results. It confirms Eqs. 4.5−4.7 effect on Eq. 4.1. The energy range within 10 meV agreement with DFT values [59, 111, 112, 87] are listed in Table. 5.2. Here, WS_2 CB has the narrowest with 70 meV and MoS_2 VB has the widest with 400 meV.

5.2 Spin-Dependent Four-Band $k{\cdot}p$ Hamiltonian

The spin-orbit interaction in TMDs is quite strong [113] in contrast to for instance, monolayer graphene and hBN [87]. This is due to the presence of heavy metal atoms inside of this materials. Spin-diagonal and wave vector-independent approximation commonly are used to incorporate the spin-dependent effects in TMDs [93, 107, 66, 110]. Thus, we first turn the two-band Hamiltonian of Eq. (4.4) into a one with spin-dependent diagonal entries form as

$$H_{\text{eff}} = \begin{pmatrix} h_{11} & h_{12} \\ h_{12}^{*} & h_{22} \end{pmatrix} \longrightarrow \quad H_{\text{eff}}^{\downarrow,\uparrow} = \begin{pmatrix} h_{11}^{\downarrow,\uparrow} & h_{12} \\ h_{12}^{*} & h_{22}^{\downarrow,\uparrow} \end{pmatrix}, \tag{5.1}$$

by adjusting only the electron-hole asymmetry input in Eq. (4.5) so that it becomes

$$H_{\text{as}}^{\downarrow,\uparrow} = k^2 \begin{pmatrix} \beta^{\downarrow,\uparrow} & 0 \\ 0 & \alpha^{\downarrow,\uparrow} \end{pmatrix}, \tag{5.2}$$

where the fitted $\beta^{\downarrow,\uparrow}$ and $\alpha^{\downarrow,\uparrow}$ to the corresponding effective mass amounts are listed in Table 5.3. We do not inflate the number of fitting parameters significantly by keeping the remaining two-band $k \cdot p$ parameters $(f_1, f_2, f_4, f_5, \kappa, \eta)$ as in Table 5.2.

With these the two-band formalism extends to both spin channels that arise into the four-band $k{\cdot}p$ Hamiltonian which is expressed in the Bloch basis ordering of $\{|\boldsymbol{k},\, d_{z^2},\uparrow\rangle\,,\, |\boldsymbol{k},\, d_{z^2},\downarrow\rangle\,,\, |\boldsymbol{k},\, d_{x^2-y^2}+id_{xy},\uparrow\rangle\,,\, |\boldsymbol{k},\, d_{x^2-y^2}+id_{xy},\downarrow\rangle\}$ as

$$H_{\text{4B}} = \begin{pmatrix} h_{11}^{\uparrow} & 0 & h_{12} & 0 \\ 0 & h_{11}^{\downarrow} & 0 & h_{12} \\ h_{12}^{*} & 0 & h_{22}^{\uparrow} & 0 \\ 0 & h_{12}^{*} & 0 & h_{22}^{\downarrow} \end{pmatrix} + \tau \begin{pmatrix} -\Delta_{\text{cb}}^{\text{so}} & 0 & 0 & 0 \\ 0 & 0 & 0 & 0 \\ 0 & 0 & -\Delta_{\text{vb}}^{\text{so}} & 0 \\ 0 & 0 & 0 & 0 \end{pmatrix}, \tag{5.3}$$

where τ is the valley index. For the $+K$ $(-K)$ valley this quantity is $+1$ (-1). $\Delta_{\text{cb}}^{\text{so}}$ $(\Delta_{\text{vb}}^{\text{so}})$ is the CB (VB) spin splitting as tabulated in Table 5.3.

Figure 5.3 demonstrates the spin-dependent band structure of different TMDs. As the spin-dependent parameters in Eq. (5.3) are located on the diagonal entries [93], spin is a good quantum label in this level of approximation.

Table 5.3: Additional spin-dependent $k \cdot p$ parameters required for the four-band Hamiltonian. CB and VB spin splittings are taken from spin-polarized DFT band structure [110]. $\alpha^{\downarrow}$ and $\beta^{\downarrow}$ values corresponds to the two-band values in Table 5.2.

TMD	MoS_2	$MoSe_2$	WS_2	WSe_2
Δ_{cb}^{so} (meV)	-3	-22	32	37
Δ_{vb}^{so} (meV)	148	186	429	466
$\alpha^{\downarrow}$ (eV·Å^2)	4.16	5.22	8.2	8.43
$\beta^{\downarrow}$ (eV·Å^2)	-2.35	-3.9	-4.43	-5.4
$\alpha^{\uparrow}$ (eV·Å^2)	4.23	5.22	8.58	8.85
$\beta^{\uparrow}$ (eV·Å^2)	-2.2	-3.86	-5.47	-6.15

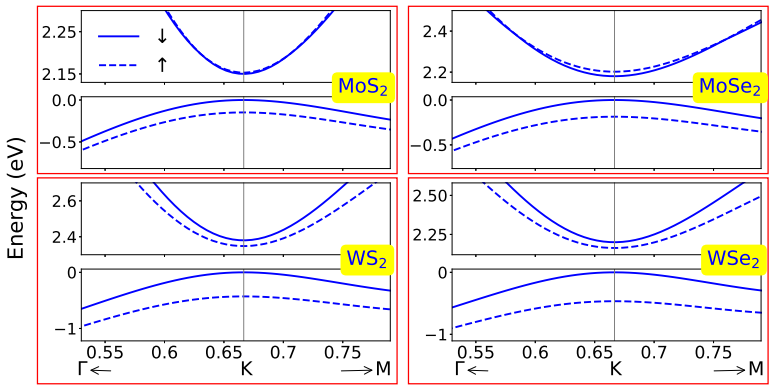

Figure 5.3: Four-band $k \cdot p$ band structure of TMDs. Solid line corresponds to spin $\downarrow$ and dashed one corresponds to spin $\uparrow$ bands. Abscissae are in units of $2\pi/a$. Spin-dependent parameters are listed in Table 5.3, and the remaining spin-independent parameters $(f_1, f_2, f_4, f_5, \kappa, \eta)$ are used from Table 5.2.

5.3 Three Band Tight Binding Model

The two-band $k \cdot p$ model is confined to the vicinity of the K points. The number of bands should be increased in order to extend this model over a wider part of the Brillouin zone [59]. The three-band tight-binding (TB) model provides a full-zone band structure that is fitted to the first-principles data. Up to third nearest neighbor interactions [107],

$$H_0 = \begin{pmatrix} V_0 & V_1 & V_2 \\ V_1^* & V_{11} & V_{12} \\ V_2^* & V_{12}^* & V_{22} \end{pmatrix}, \tag{5.4}$$

where V_0, V_1, V_2, V_{11}, V_{12}, V_{22} are the TB hopping terms. This Hamiltonian is for unstrained TMDs. To implement strain, we remedy it by the two-band deformation potentials[87],

$$H_S = \begin{pmatrix} e_a & e_b & e_b \\ e_b & -e_a & 0 \\ e_b & 0 & -e_a \end{pmatrix}, \tag{5.5}$$

where

$$e_a = f_4 \left(\varepsilon_{xx} + \varepsilon_{yy}\right), \tag{5.6}$$

$$e_b = f_5 \left(\varepsilon_{xx} - \varepsilon_{yy}\right). \tag{5.7}$$

The deformation potentials are only available for the top VB and the bottom CB [87] while the above mentioned TB is a three-band model. Therefore, we extend it to the two-dimensional subspace. Here, only the uniaxial and biaxial strain is involved, the shear strain is ignored as it only shifts the band extrema. For details refer to Chapter. 2. To confirm the validity of this simple strain recipe, we compare it with the first-principles band structure [87] for WSe_2 under $\pm$ 2% biaxial, and unstrained cases in Fig. 5.4. As it can be seen from this figure, the results agreement is quite satisfactory around the K valley, whereas away from this region (toward the Γ point) disagreement occurs. These restrictions is not a matter, as because of symmetry considerations the geometrical band properties that we are interested in are localized around the K vallry, and vanish toward the Γ point [109].

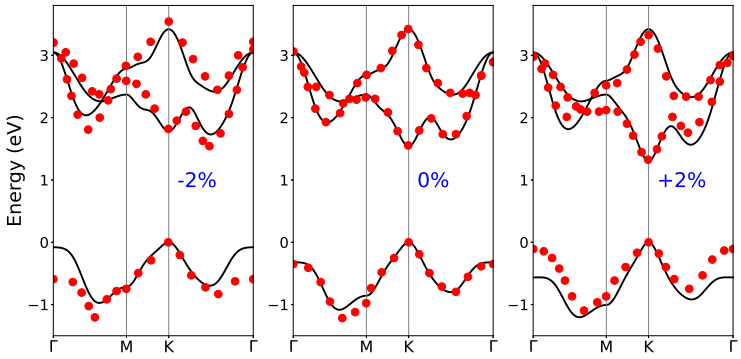

Figure 5.4: Comparison of first-principles band structure (red dots) with the TB (black line) results for WSe_2. Unstrained (0%) as well as ± 2% biaxial strain cases are shown. Energy reference is set to VB maximum for each case.

5.4 Berry Curvature and Orbital Magnetic Moment

For a wavepacket of Bloch electrons moving adiabatically in a non-degenerate energy band with index n, it is possible to have it tightly localized compared to the length scale of the external perturbation. So, it is possible to talk simultaneously about the wavevector and the position of the electron. The equations of motion for Bloch electrons in this semiclassical picture under applied electric and magnetic fields are written as [114],

$$\dot{\boldsymbol{r}} = \frac{1}{\hbar}\frac{\partial E_n(\boldsymbol{k})}{\partial \boldsymbol{k}} - \dot{\boldsymbol{k}} \times \boldsymbol{\Omega}_n(\boldsymbol{k}), \quad \hbar\dot{\boldsymbol{k}} = -e\boldsymbol{E} - e\dot{\boldsymbol{r}} \times \boldsymbol{B}. \tag{5.8}$$

Here, Ω is a pseudovector known as the Berry curvature,

$$\boldsymbol{\Omega}_n(\boldsymbol{k}) = i\frac{\hbar^2}{m_0^2}\sum_{i\neq n}\frac{\boldsymbol{P}_{n,i}(\boldsymbol{k}) \times \boldsymbol{P}_{i,n}(\boldsymbol{k})}{[E_n^0(\boldsymbol{k}) - E_i^0(\boldsymbol{k})]^2}, \tag{5.9}$$

where, $\boldsymbol{P}_{n,i}(\boldsymbol{k}) \equiv \langle u_{n,\boldsymbol{k}}|\hat{\mathcal{P}}|u_{i,\boldsymbol{k}}\rangle$ is the interband matrix element of the canonical momentum operator $\hat{\mathcal{P}}$ and $E_n^0(\boldsymbol{k})$ is the dispersion of the nth band. For an unperturbed system with time-reversal and spatial inversion symmetry, the velocity formula from Eq. (5.8) should be invariant under these operations. Under time

reversal, $\boldsymbol{v}_n$ and $\boldsymbol{k}$ change sign while $\boldsymbol{E}$ is fixed. Under spatial inversion, $\boldsymbol{v}_n$, $\boldsymbol{k}$, and $\boldsymbol{E}$ change sign. By these explanations for a system with time reversal symmetry, $\boldsymbol{\Omega}_n(-k) = -\boldsymbol{\Omega}_n(\boldsymbol{k})$ and for a system with spatial inversion symmetry, $\boldsymbol{\Omega}_n(-k) = \boldsymbol{\Omega}_n(\boldsymbol{k})$. Thus, for a system with both time-reversal and spatial inversion symmetry the Berry curvature vanishes identically throughout the Brillouin zone. For TMDs, time reversal symmetry exists but inversion symmetry is broken for K and $-K$ valleys. Therefore, in these monolayer crystals Berry curvature has finite value with opposite sign in two valleys [114].

In our 2 band$-k\cdot p$ model we have just two conduction and valence bands. Thus, $\Omega_{(c/v)}$ for conduction/valence band becomes as below,

$$\boldsymbol{\Omega}_{(c/v)}(\boldsymbol{k}) = i\frac{\hbar^2}{m_0^2}\frac{\boldsymbol{P}_{cv/vc}(\boldsymbol{k}) \times \boldsymbol{P}_{vc/cv}(\boldsymbol{k})}{[E^0_{(c/v)}(\boldsymbol{k}) - E^0_{(v/c)}(\boldsymbol{k})]^2}. \tag{5.10}$$

Dipole matrix element connecting conduction and valence states can be expressed as,

$$\mathcal{P}_\alpha(\boldsymbol{k}) \equiv \frac{m_0}{\hbar}\left\langle U_c\right| \frac{\partial \hat{H}}{\partial k_\alpha} \left|U_v\right\rangle \tag{5.11}$$

which $\alpha = x/y$. Orbital magnetic moment ($\boldsymbol{m}$) is another pseudovector which identifies K and $-K$ valleys in TMDs,

$$\boldsymbol{m}_n(\boldsymbol{k}) = -i\frac{e\hbar}{2m_0^2}\sum_{i\neq n}\frac{\boldsymbol{P}_{n,i}(\boldsymbol{k}) \times \boldsymbol{P}_{i,n}(\boldsymbol{k})}{E^0_n(\boldsymbol{k}) - E^0_i(\boldsymbol{k})}. \tag{5.12}$$

For 2band$-k\cdot p$ model it has the form as below,

$$\boldsymbol{m}_{(c/v)}(\boldsymbol{k}) = -i\frac{e\hbar}{2m_0^2}\frac{\boldsymbol{P}_{cv/vc}(\boldsymbol{k}) \times \boldsymbol{P}_{vc/cv}(\boldsymbol{k})}{E^0_{(c/v)}(\boldsymbol{k}) - E^0_{(v/c)}(\boldsymbol{k})}. \tag{5.13}$$

Combining Eq. 4.4 with Eqs. 5.10 and 5.13, we calculate Berry curvature and orbital magnetic moment. We choose monolayer WSe_2 to discuss these geometric band properties. Here the bands with the narrowest spin-allowed bandgap transition are taken into account (spin–$\downarrow$) in order to reduce the computational task to the two-band $k\cdot p$, and the three-band TB cases. Fig. 5.6 demonstrates (a) $\boldsymbol{\Omega}$ and (b) $\boldsymbol{m}$ for an unstrained WSe_2. From this figure, for both highest valence and lowest conduction bands results from TNN TB and $k\cdot p$ method are in qualitative agreement around K valley. Also, variation in both geometric varieties in TB model is wider than $k\cdot p$ method. Furthermore, it can be seen

that BC toggles sign between VB and CB but not for the OMM, together with the emphasis of TW on these.

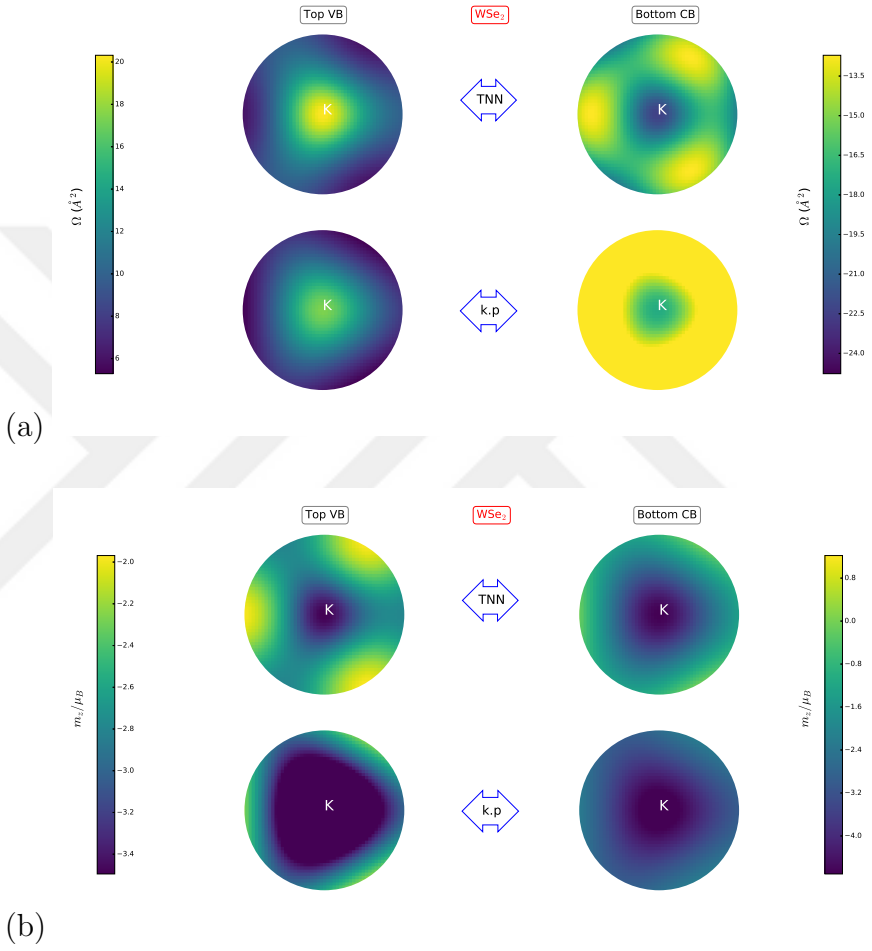

Figure 5.5: BC and (b) OMM of VB and CB for an unstrained monolayer WSe_2 showing a part of the Brillouin zone centered at the K point over a radius of $0.12 \times 2\pi/a$.

5.5 Effects of Strain on Berry Curvature and Orbital Magnetic Moment

Fig. 5.6 shows the effects of strain on the (a) $\boldsymbol{\Omega}$ and (b) $\boldsymbol{m}$ for a monolayer WSe_2. Quantities are for a continuous range of (compressive/tensile) biaxial strain in Q−K−M route within the Brillion zone. The Q point is set at the half way between the Γ and K points. From the TB results, the geometric properties around the K valley inflate as the strain type shifts from compressive to tensile. For the CB, beyond the halfway between the $Q - K$ panel the alternation gets reversed.

In the vicinity of K valley the $k{\cdot}p$ results are close to TB with lower amplitudes. Toward the M point, for both VB and CB the cubic term declines the aggrement with TB. Eventhough, for the same point it has a positive impact on the band structure(Fig. 5.2).

Fig. 5.7 demonstrates these features more clearly. Here, the continuous tunability of both BC and OMM under hydrostatic strain $\varepsilon_H = \varepsilon_{xx} + \varepsilon_{yy}$ is displayed. Around the K valley, $k \cdot p$ is in qualitative agreement with TB, while it cannot reproduce the broad variation of the OMM especially for the CB. By around $+5\%$ hydrostatic strain, the geometric band properties are doubled with respect to unstrained values.

Making use of two-band analytical expressions [62, 115] which are valid at the K point, $\Omega_z = 2f_2/E_g$, $\mu_z = \mu_B m_0/m^*$, where the strained band gap [82] $E_g = f_1 + 2f_4\varepsilon_H$, and the strained effective mass [82] $m^* = \pm\hbar^2 E_g/[2(f_2 a)^2]$, we offer a simple explanation for these amplified geometrical band properties under tensile hydrostatic strain. A tensile hydrostatic strain ($\varepsilon_H > 0$) declines the E_g as $f_4 < 0$ from table 5.2. Hence, this decline in band gap causes an increasement in both BC and OMM.

(a)

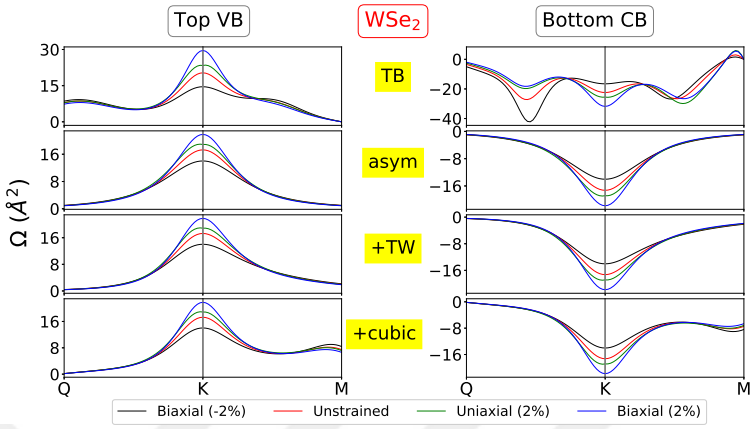

(b)

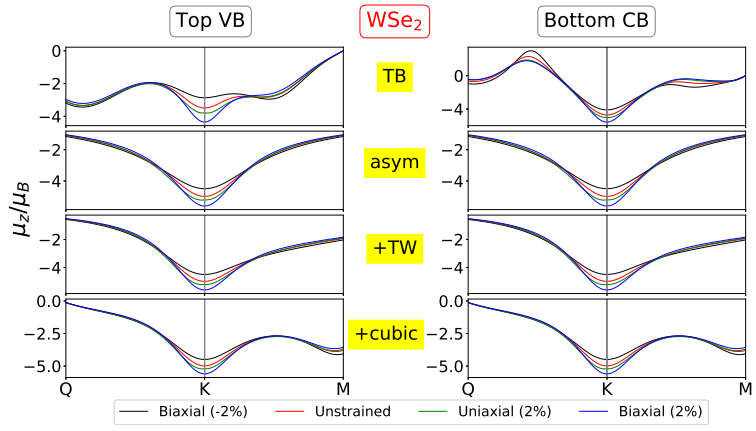

Figure 5.6: Strain effect on(a) BC and (b) OMM of VB and CB for a monolayer WSe_2 according to TB (top) and $k \cdot p$ (bottom) models. For the latter the effect of each additional term (Eqs. (4.5)−(4.7)) is shown.

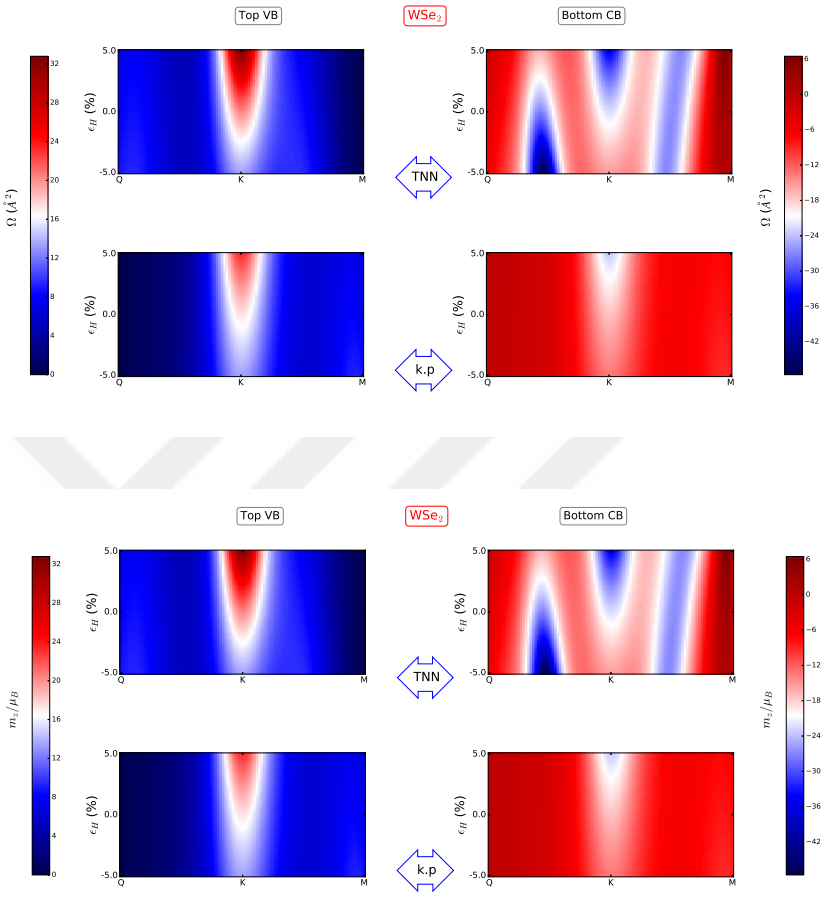

(a)

(b)

Figure 5.7: Effect of compressive and tensile hydrostatic strain on (a) BC and (b) OMM of CB and VB for WSe_2.

Chapter 6

Conclusions

In this thesis first, a simple strained two-band $k \cdot p$ approach is developed. Applying this model to TMDs shows that the bandgap and effective masses are affected by the hydrostatic component of the strain. Furthermore, it is observed that the shear strain shifts the wavevector of the valley minima, but does not change the optoelectronic properties. A mixing of the valley edge states occurs away from the extrema that is intensified (reduced) for a tensile (compressive) strain type. Comparison of strain-dependent PL peak shifts taking into account excitonic effects with a wide range of experimental data for monolayer TMDs exhibits a satisfying agreement, and it reveals whether Poissons effect takes place in a certain experiment. As another finding, circular polarization selectivity beyond the K valley transition onset can be tuned in either direction by exerting tensile or compressive strain. This is more conspicuous for the biaxial strain.

Most favorable features of TMDs can be attributed to geometric band effects controlled by BC and OMM. Moreover, they can be widely altered by applying strain. To adventure these in device applications reliable and physically-transparent band structure tools are required. In this thesis, two such models are offered. First, a new parameter set development for a (two- or a four band) $k \cdot p$ model. Second, a strained extension for a three-band TB Hamiltonian. Note that despite their simplicity, both capture the fundamental physics that carry out

the variation of BC and OMM around the K valley geometric hotspots. Under reasonable biaxial tensile strains (around 2.5%) these can be doubled in value.

6.1 Suggestions for Future Work

The strained $k \cdot p$ approach can be used for device modeling purposes of TMDs under electric, magnetic or optical excitations, as well as localized strain. Valley Hall effect (VHE) which is discussed in introduction part of this thesis is an example of valley polarization injection inside of this materials using electrical excitation [116, 117]. Also, it is possible to make inverse VHE as it has been developed in graphene [118, 119] but remains as a challenge for TMDs. Lee et. al. reported the generation of bulk valley magnetization in strained single-layer MoS_2 by charge current [116]. The inverse process of this magneto-electric effect can be a challenge in TMDs valleytronic field as well.

Excitation of TMDs by magnetic or optical means leads to emergence of particles or quasiparticles other than electrons that also possess the valley degree of freedom. For instance, when a TMD monolayer is embedded in optical microcavities, the large oscillator strengths of excitonic transitions allow the formation of polaritons that are quasiparticles [120, 121]. Use of these hybrid systems to realize valley lasers, for which gain and lasing occur only in one valley, could be another objective [122].

Due to the strain−induced modulation of the bandgap the piezoresistive effect appears in TMDs. MoS_2 has a much higher fracture strain than silicon (0.7%) [123], thus it is more suitable for use on curved surfaces for flexible strain sensors and highly deformable objects, such as biological tissue.

Bibliography

[1] K. F. Mak, C. Lee, J. Hone, J. Shan, and T. F. Heinz, "Atomically thin MoS_2: A new direct-gap semiconductor," *Physical Review Letters*, vol. 105, p. 136805, Sept. 2010.

[2] B. Radisavljevic, A. Radenovic, J. Brivio, V. Giacometti, and A. Kis, "Single-layer MoS_2 transistors," *Nature Nanotechnology*, vol. 6, p. 147, Mar. 2011.

[3] R. S. Sundaram, M. Engel, A. Lombardo, R. Krupke, A. C. Ferrari, P. Avouris, and M. Steiner, "Electroluminescence in single layer MoS_2," *Nano Letters*, vol. 13, pp. 1416–1421, Apr. 2013.

[4] X. Xu, W. Yao, D. Xiao, and T. F. Heinz, "Spin and pseudospins in layered transition metal dichalcogenides," *Nature Physics*, vol. 10, p. 343, May 2014.

[5] C. R. Zhu, G. Wang, B. L. Liu, X. Marie, X. F. Qiao, X. Zhang, X. X. Wu, H. Fan, P. H. Tan, T. Amand, and B. Urbaszek, "Strain tuning of optical emission energy and polarization in monolayer and bilayer MoS_2," *Physical Review B*, vol. 88, p. 121301, Sept. 2013.

[6] M. Manca, M. M. Glazov, C. Robert, F. Cadiz, T. Taniguchi, K. Watanabe, E. Courtade, T. Amand, P. Renucci, X. Marie, G. Wang, and B. Urbaszek, "Enabling valley selective exciton scattering in monolayer WSe_2 through upconversion," *Nature Communications*, vol. 8, p. 14927, Apr. 2017.

[7] K. F. Mak, K. He, C. Lee, G. H. Lee, J. Hone, T. F. Heinz, and J. Shan, "Tightly bound trions in monolayer MoS_2," *Nature Materials*, vol. 12, pp. 207–211, Mar. 2013.

[8] K. He, N. Kumar, L. Zhao, Z. Wang, K. F. Mak, H. Zhao, and J. Shan, "Tightly bound excitons in monolayer WSe_2," *Physical Review Letters*, vol. 113, p. 026803, July 2014.

[9] K. He, C. Poole, K. F. Mak, and J. Shan, "Experimental demonstration of continuous electronic structure tuning via strain in atomically thin MoS_2," *Nano Letters*, vol. 13, pp. 2931–2936, June 2013.

[10] G. Aivazian, Z. Gong, A. M. Jones, R.-L. Chu, J. Yan, D. G. Mandrus, C. Zhang, D. Cobden, W. Yao, and X. Xu, "Magnetic control of valley pseudospin in monolayer WSe_2," *Nature Physics*, vol. 11, p. 148, Feb. 2015.

[11] D. Akinwande, N. Petrone, and J. Hone, "Two-dimensional flexible nanoelectronics," *Nature Communications*, vol. 5, p. 5678, Dec. 2014.

[12] H. J. Conley, B. Wang, J. I. Ziegler, R. F. Haglund, S. T. Pantelides, and K. I. Bolotin, "Bandgap engineering of strained monolayer and bilayer MoS_2," *Nano Letters*, vol. 13, pp. 3626–3630, Aug. 2013.

[13] D. Lloyd, X. Liu, J. W. Christopher, L. Cantley, A. Wadehra, B. L. Kim, B. B. Goldberg, A. K. Swan, and J. S. Bunch, "Band gap engineering with ultralarge biaxial strains in suspended monolayer MoS_2," *Nano Letters*, vol. 16, pp. 5836–5841, Sept. 2016.

[14] A. Castellanos-Gomez, R. Roldn, E. Cappelluti, M. Buscema, F. Guinea, H. S. J. van der Zant, and G. A. Steele, "Local strain engineering in atomically thin MoS_2," *Nano Letters*, vol. 13, pp. 5361–5366, Nov. 2013.

[15] Y. Y. Hui, X. Liu, W. Jie, N. Y. Chan, J. Hao, Y.-T. Hsu, L.-J. Li, W. Guo, and S. P. Lau, "Exceptional tunability of band energy in a compressively strained trilayer MoS_2 sheet," *ACS Nano*, vol. 7, pp. 7126–7131, Aug. 2013.

[16] G. Plechinger, A. Castellanos-Gomez, M. Buscema, H. S. J. v. d. Zant, G. A. Steele, A. Kuc, T. Heine, C. Schller, and T. Korn, "Control of biaxial strain

in single-layer molybdenite using local thermal expansion of the substrate," *2D Materials*, vol. 2, no. 1, p. 015006, 2015.

[17] H. Li, A. W. Contryman, X. Qian, S. M. Ardakani, Y. Gong, X. Wang, J. M. Weisse, C. H. Lee, J. Zhao, P. M. Ajayan, J. Li, H. C. Manoharan, and X. Zheng, "Optoelectronic crystal of artificial atoms in strain-textured molybdenum disulphide," *Nature Communications*, vol. 6, p. 7381, June 2015.

[18] S. B. Desai, G. Seol, J. S. Kang, H. Fang, C. Battaglia, R. Kapadia, J. W. Ager, J. Guo, and A. Javey, "Strain-Induced indirect to direct bandgap transition in multilayer WSe_2," *Nano Letters*, vol. 14, pp. 4592–4597, Aug. 2014.

[19] Y. Wang, C. Cong, W. Yang, J. Shang, N. Peimyoo, Y. Chen, J. Kang, J. Wang, W. Huang, and T. Yu, "Strain-induced direct-indirect bandgap transition and phonon modulation in monolayer WS_2," *Nano Research*, vol. 8, pp. 2562–2572, Aug. 2015.

[20] S. Yang, C. Wang, H. Sahin, H. Chen, Y. Li, S.-S. Li, A. Suslu, F. M. Peeters, Q. Liu, J. Li, and S. Tongay, "Tuning the optical, magnetic, and electrical properties of $ReSe_2$ by nanoscale strain engineering," *Nano Letters*, vol. 15, pp. 1660–1666, Mar. 2015.

[21] R. Schmidt, I. Niehues, R. Schneider, M. Drppel, T. Deilmann, Michael Rohlfing, S. M. d. Vasconcellos, A. Castellanos-Gomez, and R. Bratschitsch, "Reversible uniaxial strain tuning in atomically thin WSe_2," *2D Materials*, vol. 3, no. 2, p. 021011, 2016.

[22] J. O. Island, A. Kuc, E. H. Diependaal, R. Bratschitsch, H. S. J. v. d. Zant, T. Heine, and A. Castellanos-Gomez, "Precise and reversible band gap tuning in single-layer $MoSe_2$ by uniaxial strain," *Nanoscale*, vol. 8, pp. 2589–2593, Jan. 2016.

[23] H. Peelaers and C. G. Van de Walle, "Effects of strain on band structure and effective masses in MoS_2," *Physical Review B*, vol. 86, p. 241401, Dec. 2012.

[24] P. Lu, X. Wu, W. Guo, and X. C. Zeng, "Strain-dependent electronic and magnetic properties of MoS_2 monolayer, bilayer, nanoribbons and nanotubes," *Physical Chemistry Chemical Physics*, vol. 14, pp. 13035–13040, Aug. 2012.

[25] P. Johari and V. B. Shenoy, "Tuning the electronic properties of semiconducting transition metal dichalcogenides by applying mechanical strains," *ACS Nano*, vol. 6, pp. 5449–5456, June 2012.

[26] E. Scalise, M. Houssa, G. Pourtois, V. Afanasev, and A. Stesmans, "Strain-induced semiconductor to metal transition in the two-dimensional honeycomb structure of MoS_2," *Nano Research*, vol. 5, pp. 43–48, Jan. 2012.

[27] H. Pan and Y.-W. Zhang, "Tuning the electronic and magnetic properties of MoS_2 nanoribbons by strain engineering," *The Journal of Physical Chemistry C*, vol. 116, pp. 11752–11757, May 2012.

[28] J. Feng, X. Qian, C.-W. Huang, and J. Li, "Strain-engineered artificial atom as a broad-spectrum solar energy funnel," *Nature Photonics*, vol. 6, pp. 866–872, Dec. 2012.

[29] H. Shi, H. Pan, Y.-W. Zhang, and B. I. Yakobson, "Quasiparticle band structures and optical properties of strained monolayer MoS_2 and WS_2," *Physical Review B*, vol. 87, p. 155304, Apr. 2013.

[30] M. Ghorbani-Asl, S. Borini, A. Kuc, and T. Heine, "Strain-dependent modulation of conductivity in single-layer transition-metal dichalcogenides," *Physical Review B*, vol. 87, p. 235434, June 2013.

[31] E. Scalise, M. Houssa, G. Pourtois, V. V. Afanasev, and A. Stesmans, "First-principles study of strained 2d MoS_2," *Physica E: Low-dimensional Systems and Nanostructures*, vol. 56, pp. 416–421, Feb. 2014.

[32] D. M. Guzman and A. Strachan, "Role of strain on electronic and mechanical response of semiconducting transition-metal dichalcogenide monolayers: An ab-initio study," *Journal of Applied Physics*, vol. 115, p. 243701, June 2014.

[33] H. Rostami, R. Roldn, E. Cappelluti, R. Asgari, and F. Guinea, "Theory of strain in single-layer transition metal dichalcogenides," *Physical Review B*, vol. 92, p. 195402, Nov. 2015.

[34] Y.-p. Miao, F. Ma, Y.-h. Huang, and K.-w. Xu, "Strain effects on electronic states and lattice vibration of monolayer MoS_2," *Physica E: Low-dimensional Systems and Nanostructures*, vol. 71, pp. 1–6, July 2015.

[35] M. Hosseini, M. Elahi, M. Pourfath, and D. Esseni, "Strain-induced modulation of electron mobility in single-layer transition metal dichalcogenides MX_2 (M = Mo , W; X = S, Se)," *IEEE Transactions on Electron Devices*, vol. 62, pp. 3192–3198, Oct. 2015.

[36] A. E. Maniadaki, G. Kopidakis, and I. N. Remediakis, "Strain engineering of electronic properties of transition metal dichalcogenide monolayers," *Solid State Communications*, vol. 227, pp. 33–39, Feb. 2016.

[37] Y. Zhao, Z. Zhang, and G. Ouyang, "Lattice strain effect on the band offset in single-layer MoS_2: An atomic-bond-relaxation approach," *The Journal of Physical Chemistry C*, vol. 121, pp. 5366–5371, Mar. 2017.

[38] M. Feierabend, A. Morlet, G. Berghuser, and E. Malic, "Impact of strain on the optical fingerprint of monolayer transition-metal dichalcogenides," *Physical Review B*, vol. 96, p. 045425, July 2017.

[39] C. Palacios-Berraquero, D. M. Kara, A. R.-P. Montblanch, M. Barbone, P. Latawiec, D. Yoon, A. K. Ott, M. Loncar, A. C. Ferrari, and M. Atatüre, "Large-scale quantum-emitter arrays in atomically thin semiconductors," *Nat. Commun.*, vol. 8, p. 15093, 2017.

[40] A. Branny, G. Wang, S. Kumar, C. Robert, B. Lassagne, X. Marie, B. D. Gerardot, and B. Urbaszek, "Discrete quantum dot like emitters in monolayer $MoSe_2$: Spatial mapping, magneto-optics, and charge tuning," *Appl. Phys. Lett.*, vol. 108, p. 142101, 2016.

[41] M. M. Ugeda, A. J. Bradley, S.-F. Shi, F. H. d. Jornada, Y. Zhang, D. Y. Qiu, W. Ruan, S.-K. Mo, Z. Hussain, Z.-X. Shen, F. Wang, S. G. Louie, and

M. F. Crommie, "Giant bandgap renormalization and excitonic effects in a monolayer transition metal dichalcogenide semiconductor," *Nature Materials*, vol. 13, p. 1091, Dec. 2014.

[42] D. Y. Qiu, F. H. da Jornada, and S. G. Louie, "Optical spectrum of MoS_2: Many-Body effects and diversity of exciton states," *Physical Review Letters*, vol. 111, p. 216805, Nov. 2013.

[43] G. D. Scholes and G. Rumbles, "Excitons in nanoscale systems," *Nature Materials*, vol. 5, p. 683, Sept. 2006.

[44] A. Esser, E. Runge, R. Zimmermann, and W. Langbein, "Photoluminescence and radiative lifetime of trions in GaAs quantum wells," *Physical Review B*, vol. 62, pp. 8232–8239, Sept. 2000.

[45] J. Jadczak, L. Bryja, K. Ryczko, M. Kubisa, A. Wjs, M. Potemski, F. Liu, D. R. Yakovlev, M. Bayer, C. A. Nicoll, I. Farrer, and D. A. Ritchie, "High magnetic field studies of charged exciton localization in $GaAs/Al_xGa_{1-x}As$ quantum wells," *Applied Physics Letters*, vol. 105, p. 112104, Sept. 2014.

[46] J. Xiao, M. Zhao, Y. Wang, and X. Zhang, "Excitons in atomically thin 2d semiconductors and their applications," *Nanophotonics*, vol. 6, no. 6, pp. 1309–1328, 2017.

[47] Y. G. Semenov and K. W. Kim, "Bias-driven spontaneous spin-valley polarization in monolayer transition-metal dichalcogenides," *Physical Review B*, vol. 93, p. 041414, Jan. 2016.

[48] B. Liu, C. Zhu, E. Wang, G. Wang, H. Ye, J. Feng, J. Shi, P. Tan, Q. Niu, T. Cao, and W. Han, "Valley-selective circular dichroism of monolayer molybdenum disulphide," *Nature Communications*, vol. 3, p. 887, June 2012.

[49] J. R. Schaibley, H. Yu, G. Clark, P. Rivera, J. S. Ross, K. L. Seyler, W. Yao, and X. Xu, "Valleytronics in 2D materials," *Nature Reviews Materials*, vol. 1, p. 16055, 2016.

[50] M. Yamamoto, Y. Shimazaki, I. V. Borzenets, and S. Tarucha, "Valley hall effect in two-dimensional hexagonal lattices," *Journal o the Physical Society of Japan*, vol. 84, p. 121006, 2015.

[51] D. V. Vanderbilt, *Berry phases in electronic structure theory*. Cambridge University Press, Cambridge, 2018.

[52] D. Xiao, M. C. Chang, and Q. Niu, "Berry phase effects on electronic properties," *Reviews of Modern Physics*, vol. 82, pp. 1959–2007, July 2010.

[53] X. Zhang, W.-Y. Shan, and D. Xiao, "Optical selection rule of excitons in gapped chiral fermion systems," *Physical Review Letters*, vol. 120, p. 077401, 2018.

[54] T. Cao, M. Wu, and S. G. Louie, "Unifying optical selection rules for excitons in two dimensions: Band topology and winding numbers," *Physical Review Letters*, vol. 120, p. 077401, 2018.

[55] A. Srivastava, M. Sidler, A. V. Allain, D. S. Lembke, A. Kis, and A. Imamolu, "Valley Zeeman effect in elementary optical excitations of monolayer WSe_2," *Nature Physics*, vol. 11, pp. 141–147, Feb. 2015.

[56] J. Zhou, W.-Y. Shan, W. Yao, and D. Xiao, "Berry phase modification to the energy spectrum of excitons," *Physical Review Letters*, vol. 115, p. 166803, 2015.

[57] M.-C. Chang and Q. Niu, "Berry curvature, orbital moment, and effective quantum theory of electrons in electromagnetic fields," *Journal of Physics: Condensed Matter*, vol. 20, p. 193202, 2008.

[58] M. Brooks and G. Burkard, "Spin-degenerate regimes for single quantum dots in transition metal dichalcogenide monolayers," *Physical Review B*, vol. 95, p. 245411, 2017.

[59] D. V. Rybkovskiy, I. C. Gerber, and M. V. Durnev, "Atomically inspired $k.p$ approach and valley Zeeman effect in transition metal dichalcogenide monolayers," *Physical Review B*, vol. 95, p. 155406, Apr. 2017.

[60] G. Aivazian, Z. Gong, A. M. Jones, R.-L. Chu, J. Yan, D. G. Mandrus, C. Zhang, D. Cobden, W. Yao, and X. Xu, "Magnetic control of valley pseudospin in monolayer WSe_2," *Nature Physics*, vol. 11, pp. 148–152, Feb. 2015.

[61] M. Schüler, U. D. Giovannini, H. Hübener, A. Rubio, M. A. Sentef, and P. Werner, "Local berry curvature signatures in dichroic angle-resolved photoelectron spectroscopy," *arXiv preprint arXiv:1905.09404*, 2019.

[62] D. Xiao, W. Yao, and Q. Niu, "Valley-contrasting physics in graphene: Magnetic moment and topological transport," *Physical Review Letters*, vol. 99, p. 236809, Dec. 2007.

[63] S.-Y. Chen, Z. Lu, T. Goldstein, J. Tong, A. Chaves, J. Kunstmann, L. S. R. Cavalcante, T. Woźniak, G. Seifert, D. R. Reichman, T. Taniguchi, K. Watanabe, D. Smirnov, and J. Yan, "Luminescent emission of excited rydberg excitons from monolayer WSe_2," *Nano Letters*, vol. 19, pp. 2464–2471, Apr. 2019.

[64] S. Fang, S. Carr, M. A. Cazalilla, and E. Kaxiras, "Electronic structure theory of strained two-dimensional materials with hexagonal symmetry," *Physical Review B*, vol. 98, Aug. 2018.

[65] E. Cappelluti, R. Roldn, J. A. Silva-Guilln, P. Ordejn, and F. Guinea, "Tight-binding model and direct-gap/indirect-gap transition in single-layer and multilayer MoS_2," *Physical Review B*, vol. 88, p. 075409, Aug. 2013.

[66] A. Kormányos, V. Zólyomi, N. D. Drummond, P. Rakyta, G. Burkard, and V. I. Falko, "Monolayer MoS_2: Trigonal warping, the Γ valley, and spin-orbit coupling effects," *Physical Review B*, vol. 88, p. 045416, Jul 2013.

[67] T. C. Berkelbach, M. S. Hybertsen, and D. R. Reichman, "Theory of neutral and charged excitons in monolayer transition metal dichalcogenides," *Physical Review B*, vol. 88, p. 045318, July 2013.

[68] J. L. Feldman, "Elastic constants of 2h-MoS_2 and 2h-$NbSe_2$ extracted from measured dispersion curves and linear compressibilities," *Journal of Physics and Chemistry of Solids*, vol. 37, pp. 1141–1144, Jan. 1976.

[69] S. Bertolazzi, J. Brivio, and A. Kis, "Stretching and breaking of ultrathin MoS_2," *ACS nano*, vol. 5, pp. 9703–9709, Dec. 2011.

[70] M. R. Lovell, M. M. Khonsari, and R. D. Marangoni, "A finite element analysis of the frictional forces between a cylindrical bearing element and MoS_2 coated and uncoated surfaces," *Wear*, vol. 194, pp. 60–70, June 1996.

[71] A. CastellanosGomez, M. Poot, G. A. Steele, H. S. J. v. d. Zant, N. Agrat, and G. RubioBollinger, "Elastic properties of freely suspended MoS_2 nanosheets," *Advanced Materials*, vol. 24, pp. 772–775, Feb. 2012.

[72] K. Liu, Q. Yan, M. Chen, W. Fan, Y. Sun, J. Suh, D. Fu, S. Lee, J. Zhou, S. Tongay, J. Ji, J. B. Neaton, and J. Wu, "Elastic properties of chemical-vapor-deposited monolayer MoS_2, WS_2, and their bilayer heterostructures," *Nano Letters*, vol. 14, pp. 5097–5103, Sept. 2014.

[73] R. Zhang, V. Koutsos, and R. Cheung, "Elastic properties of suspended multilayer WSe_2," *Applied Physics Letters*, vol. 108, p. 042104, Jan. 2016.

[74] Z. Fan, Z. Wei-Bing, and T. Bi-Yu, "Electronic structures and elastic properties of monolayer and bilayer transition metal dichalcogenides MX_2 (M = Mo, W; X = O, S, Se, Te): A comparative first-principles study," *Chinese Physics B*, vol. 24, no. 9, p. 097103, 2015.

[75] R. Roldán, A. Castellanos-Gomez, E. Cappelluti, and F. Guinea, "Strain engineering in semiconducting two-dimensional crystals," *Journal of Physics :Condensed Matter*, vol. 27, no. 31, p. 313201, 2015.

[76] J. F. Nye, *Physical properties of crystals: their representation by tensors and matrices*. Oxford University Press, 1985.

[77] S. Bertolazzi, J. Brivio, and A. Kis, "Stretching and breaking of ultrathin MoS_2," *ACS Nano*, vol. 5, no. 12, pp. 9703–9709, 2011.

[78] D. Akinwande, N. Petrone, and J. Hone, "Two-dimensional flexible nanoelectronics," *Nat. Commun.*, vol. 5, p. 5678, 2014.

[79] P. Tonndorf, R. Schmidt, P. Böttger, X. Zhang, J. Börner, A. Liebig, M. Albrecht, C. Kloc, O. Gordan, D. R. T. Zahn, S. M. de Vasconcellos, and R. Bratschitsch, "Photoluminescence emission and raman response of monolayer MoS_2, $MoSe_2$, and WSe_2," *Optics Express*, vol. 21, pp. 4908–4916, Feb 2013.

[80] D. Sercombe, S. Schwarz, O. Del Pozo-Zamudio, F. Liu, B. J. Robinson, E. A. Chekhovich, I. I. Tartakovskii, O. Kolosov, and A. I. Tartakovskii, "Optical investigation of the natural electron doping in thin MoS_2 films deposited on dielectric substrates," *Sci. Rep.*, vol. 3, p. 3489, 2013.

[81] T. Cao, G. Wang, W. Han, H. Ye, C. Zhu, J. Shi, Q. Niu, P. Tan, E. Wang, B. Liu, and J. Feng, "Valley-selective circular dichroism of monolayer molybdenum disulphide," *Nature Communications*, vol. 3, p. 887, June 2012.

[82] S. Aas and C. Bulutay, "Strain dependence of photoluminescence and circular dichroism in transition metal dichalcogenides: a $k \cdot p$ analysis," *Optics Express*, vol. 26, pp. 28672–28681, Oct. 2018.

[83] D. Xiao, G.-B. Liu, W. Feng, X. Xu, and W. Yao, "Coupled spin and valley physics in monolayers of MoS_2 and other group-VI dichalcogenides," *Phys. Rev. Lett.*, vol. 108, p. 196802, May 2012.

[84] P. Cudazzo, I. V. Tokatly, and A. Rubio, "Dielectric screening in two-dimensional insulators: Implications for excitonic and impurity states in graphane," *Physical Review B*, vol. 84, p. 085406, Aug. 2011.

[85] Q. Zhang, Z. Chang, G. Xu, Z. Wang, Y. Zhang, Z.-Q. Xu, S. Chen, Q. Bao, J. Z. Liu, Y.-W. Mai, *et al.*, "Strain relaxation of monolayer WS_2 on plastic substrate," *Advanced Functional Materials*, vol. 26, no. 47, pp. 8707–8714, 2016.

[86] R. Frisenda, R. Schmidt, S. M. de Vasconcellos, R. Bratschitsch, D. P. de Lara, and A. Castellanos-Gomez, "Biaxial strain in atomically thin transition metal dichalcogenides," *arXiv:1804.11095 [cond-mat]*, Apr. 2018. arXiv: 1804.11095.

[87] S. Fang, S. Carr, M. A. Cazalilla, and E. Kaxiras, "Electronic structure theory of strained two-dimensional materials with hexagonal symmetry," *Physical Review B*, vol. 98, Aug. 2018.

[88] D. MacNeill, C. Heikes, K. F. Mak, Z. Anderson, A. Kormnyos, V. Zlyomi, J. Park, and D. C. Ralph, "Breaking of valley degeneracy by magnetic field in monolayer $MoSe_2$," *Physical Review Letters*, vol. 114, p. 037401, Jan. 2015.

[89] Y. Li, J. Ludwig, T. Low, A. Chernikov, X. Cui, G. Arefe, Y. D. Kim, A. M. van der Zande, A. Rigosi, H. M. Hill, S. H. Kim, J. Hone, Z. Li, D. Smirnov, and T. F. Heinz, "Valley splitting and polarization by the zeeman effect in monolayer $MoSe_2$," *Physical Review Letters*, vol. 113, p. 266804, Dec. 2014.

[90] Y. J. Zhang, T. Oka, R. Suzuki, J. T. Ye, and Y. Iwasa, "Electrically switchable chiral light-emitting transistor," *Science*, vol. 344, pp. 725–728, May 2014.

[91] R. Winkler, *Spin-Orbit Coupling Effects in Two-Dimensional Electron and Hole Systems*. Springer, Berlin, 2003.

[92] W. Yao, D. Xiao, and Q. Niu, "Valley-dependent optoelectronics from inversion symmetry breaking," *Physical Review B*, vol. 77, p. 235406, June 2008.

[93] D. Xiao, G.-B. Liu, W. Feng, X. Xu, and W. Yao, "Coupled spin and valley physics in monolayers of MoS_2 and other group-VI dichalcogenides," *Physical Review Letters*, vol. 108, p. 196802, May 2012.

[94] Z. Song, R. Quhe, S. Liu, Y. Li, J. Feng, Y. Yang, J. Lu, and J. Yang, "Tunable valley polarization and valley orbital magnetic moment Hall effect in honeycomb systems with broken inversion symmetry," *Scientific Reports*, vol. 5, p. 13906, Sept. 2015.

[95] X. Chen, L. Zhong, X. Li, and J. Qi, "Valley splitting in the transition-metal dichalcogenide monolayer via atom adsorption," *Nanoscale*, vol. 9, pp. 2188–2194, Feb. 2017.

[96] T. Cao, G. Wang, W. Han, H. Ye, C. Zhu, J. Shi, Q. Niu, P. Tan, E. Wang, B. Liu, and J. Feng, "Valley-selective circular dichroism of monolayer molybdenum disulphide," *Nat. Commun.*, vol. 3, p. 887, June 2012.

[97] X. Xu, W. Yao, D. Xiao, and T. F. Heinz, "Spin and pseudospins in layered transition metal dichalcogenides," *Nature Physics*, vol. 10, pp. 343–350, May 2014.

[98] K. F. Mak, K. He, J. Shan, and T. F. Heinz, "Control of valley polarization in monolayer MoS_2 by optical helicity," *Nature Nanotechnology*, vol. 7, pp. 494–498, Aug. 2012.

[99] A. M. Jones, H. Yu, N. J. Ghimire, S. Wu, G. Aivazian, J. S. Ross, B. Zhao, J. Yan, D. G. Mandrus, D. Xiao, W. Yao, and X. Xu, "Optical generation of excitonic valley coherence in monolayer WSe_2," *Nature Nanotechnology*, vol. 8, pp. 634–638, Sept. 2013.

[100] G. Kioseoglou, A. T. Hanbicki, M. Currie, A. L. Friedman, D. Gunlycke, and B. T. Jonker, "Valley polarization and intervalley scattering in monolayer MoS2," *Applied Physics Letters*, vol. 101, p. 221907, Nov. 2012.

[101] E. J. Sie, J. W. McIver, Y.-H. Lee, L. Fu, J. Kong, and N. Gedik, "Valley-selective optical Stark effect in monolayer WS_2," *Nature Materials*, vol. 14, pp. 290–294, Mar. 2015.

[102] G. Sallen, L. Bouet, X. Marie, G. Wang, C. R. Zhu, W. P. Han, Y. Lu, P. H. Tan, T. Amand, B. L. Liu, and B. Urbaszek, "Robust optical emission polarization in MoS_2 monolayers through selective valley excitation," *Physical Review B*, vol. 86, p. 081301, Aug. 2012.

[103] K. F. Mak, K. L. McGill, J. Park, and P. L. McEuen, "The valley Hall effect in MoS2 transistors," *Science*, vol. 344, pp. 1489–1492, June 2014.

[104] N. Ubrig, S. Jo, M. Philippi, D. Costanzo, H. Berger, A. B. Kuzmenko, and A. F. Morpurgo, "Microscopic Origin of the Valley Hall Effect in Transition Metal Dichalcogenides Revealed by Wavelength-Dependent Mapping," *Nano Letters*, vol. 17, pp. 5719–5725, Sept. 2017.

[105] B. T. Zhou, K. Taguchi, Y. Kawaguchi, Y. Tanaka, and K. T. Law, "Spin-orbit coupling induced valley Hall effects in transition-metal dichalcogenides," *Communications Physics*, vol. 2, p. 26, Mar. 2019.

[106] S. Aas and C. Bulutay, "Geometric band properties in strained monolayer transition metal dichalcogenides using simple band structures," *Journal of Applied Physics*, vol. 126, p. 115701, Sept. 2019.

[107] G. B. Liu, W. Y. Shan, Y. Yao, W. Yao, and D. Xiao, "Three-band tight-binding model for monolayers of group-VIB transition metal dichalcogenides," *Physical Review B*, vol. 88, p. 085433, Aug. 2013.

[108] G. Wang, A. Chernikov, M. M. Glazov, T. F. Heinz, X. Marie, T. Amand, and B. Urbaszek, "Colloquium: Excitons in atomically thin transition metal dichalcogenides," *Reviews of Modern Physics*, vol. 90, p. 021001, Apr. 2018.

[109] W. Feng, Y. Yao, W. Zhu, J. Zhou, W. Yao, and D. Xiao, "Intrinsic spin Hall effect in monolayers of group-VI dichalcogenides: A first-principles study," *Physical Review B*, vol. 86, p. 165108, Oct. 2012.

[110] A. Kormányos, G. Burkard, M. Gmitra, J. Fabian, V. Zólyomi, N. D. Drummond, and V. I. Fal'ko, "$k \cdot p$ theory for two-dimensional transition metal dichalcogenide semiconductors," *2D Materials*, vol. 2, p. 022001, Apr. 2015.

[111] J. Jeong, Y.-H. Choi, K. Jeong, H. Park, D. Kim, and M.-H. Cho, "Evolution of the broadband optical transition in large-area $MoSe_2$," *Physical Review B*, vol. 97, p. 075433, Feb. 2018.

[112] L. Zhang, Y. Huang, Q. Zhao, L. Zhu, Z. Yao, Y. Zhou, W. Du, and X. Xu, "Terahertz surface emission of *d*-band electrons from a layered tungsten disulfide crystal by the surface field," *Physical Review B*, vol. 96, p. 155202, Oct. 2017.

[113] A. J. Pearce, E. Mariani, and G. Burkard, "Tight-binding approach to strain and curvature in monolayer transition-metal dichalcogenides," *Physical Review B*, vol. 94, p. 155416, 2016.

[114] D. Xiao, M.-C. Chang, and Q. Niu, "Berry phase effects on electronic properties," *Reviews of Modern Physics*, vol. 82, pp. 1959–2007, July 2010.

[115] S.-Y. Chen, Z. Lu, T. Goldstein, J. Tong, A. Chaves, J. Kunstmann, L. S. R. Cavalcante, T. Woniak, G. Seifert, D. R. Reichman, T. Taniguchi, K. Watanabe, D. Smirnov, and J. Yan, "Luminescent emission of excited Rydberg excitons from monolayer WSe_2," *Nano Letters*, vol. 19, no. 4, pp. 2464–2471, 2019.

[116] J. Lee, Z. Wang, H. Xie, K. F. Mak, and J. Shan, "Valley magnetoelectricity in single-layer MoS_2," *Nature Materials*, vol. 16, pp. 887–891, Sept. 2017.

[117] Y. Ye, J. Xiao, H. Wang, Z. Ye, H. Zhu, M. Zhao, Y. Wang, J. Zhao, X. Yin, and X. Zhang, "Electrical generation and control of the valley carriers in a monolayer transition metal dichalcogenide," *Nature Nanotechnology*, vol. 11, pp. 598–602, July 2016.

[118] Y. Shimazaki, M. Yamamoto, I. V. Borzenets, K. Watanabe, T. Taniguchi, and S. Tarucha, "Generation and detection of pure valley current by electrically induced Berry curvature in bilayer graphene," *Nature Physics*, vol. 11, pp. 1032–1036, Dec. 2015.

[119] M. Sui, G. Chen, L. Ma, W.-Y. Shan, D. Tian, K. Watanabe, T. Taniguchi, X. Jin, W. Yao, D. Xiao, and Y. Zhang, "Gate-tunable topological valley transport in bilayer graphene," *Nature Physics*, vol. 11, pp. 1027–1031, Dec. 2015.

[120] Y.-J. Chen, J. D. Cain, T. K. Stanev, V. P. Dravid, and N. P. Stern, "Valley-polarized exciton−−polaritons in a monolayer semiconductor," *Nature Photonics*, vol. 11, pp. 431–435, July 2017.

[121] S. Dufferwiel, T. P. Lyons, D. D. Solnyshkov, A. a. P. Trichet, F. Withers, S. Schwarz, G. Malpuech, J. M. Smith, K. S. Novoselov, M. S. Skolnick, D. N. Krizhanovskii, and A. I. Tartakovskii, "Valley-addressable polaritons in atomically thin semiconductors," *Nature Photonics*, vol. 11, pp. 497–501, Aug. 2017.

[122] K. F. Mak, D. Xiao, and J. Shan, "Light-valley interactions in 2d semiconductors," vol. 12, pp. 451–460, 2018.

[123] K. E. Petersen, "Silicon as a mechanical material," *Proceedings of the IEEE*, vol. 70, pp. 420–457, May 1982.